



Defense Threat Reduction Agency  
8725 John J. Kingman Road, MS  
6201 Fort Belvoir, VA 22060-6201



DTRA-TR-16-66

# TECHNICAL REPORT

## UV/IR filaments for high resolution novel spectroscopic Interrogation of Plumes on nuclear materials

Distribution Statement A. Approved for public release; distribution is unlimited.

June 2016

HDTRA1-11-1-0043

Jean-Claude et al.

Prepared by:  
University of New Mexico  
1700 Lomas Blvd. NE  
Albuquerque, NM 87106

DESTRUCTION NOTICE:

Destroy this report when it is no longer needed.  
Do not return to sender.

PLEASE NOTIFY THE DEFENSE THREAT REDUCTION  
AGENCY, ATTN: DTRIAC/ J9STT, 8725 JOHN J. KINGMAN ROAD,  
MS-6201, FT BELVOIR, VA 22060-6201, IF YOUR ADDRESS  
IS INCORRECT, IF YOU WISH IT DELETED FROM THE  
DISTRIBUTION LIST, OR IF THE ADDRESSEE IS NO  
LONGER EMPLOYED BY YOUR ORGANIZATION.

# REPORT DOCUMENTATION PAGE

Form Approved  
OMB No. 0704-0188

The public reporting burden for this collection of information is estimated to average 1 hour per response, including the time for reviewing instructions, searching existing data sources, gathering and maintaining the data needed, and completing and reviewing the collection of information. Send comments regarding this burden estimate or any other aspect of this collection of information, including suggestions for reducing the burden, to Department of Defense, Washington Headquarters Services, Directorate for Information Operations and Reports (0704-0188), 1215 Jefferson Davis Highway, Suite 1204, Arlington, VA 22202-4302. Respondents should be aware that notwithstanding any other provision of law, no person shall be subject to any penalty for failing to comply with a collection of information if it does not display a currently valid OMB control number.

1. REPORT DATE (DD-MM-YYYY) 00-06-2016			2. REPORT TYPE Final		3. DATES COVERED (From - To) 06/20/2011 - 02/19/2015	
4. TITLE AND SUBTITLE UV/IR filaments for high resolution novel spectroscopic \\ Interrogation of Plumes on nuclear materials					5a. CONTRACT NUMBER	
					5b. GRANT NUMBER HDTRA1-11-1-0043	
					5c. PROGRAM ELEMENT NUMBER	
6. AUTHOR(S) Diels, Jean-Claude      Lead principal investigator Arissian, Ladan      Co-principal investigator Lenzner, Matthias      Subcontractor (Lenzner Research) Adam Hecht      Faculty					5d. PROJECT NUMBER	
					5e. TASK NUMBER	
					5f. WORK UNIT NUMBER	
7. PERFORMING ORGANIZATION NAME(S) AND ADDRESS(ES) University of New Mexico 1700 Lomas Blvd NE Albuquerque, NM 87106-3807					8. PERFORMING ORGANIZATION REPORT NUMBER	
9. SPONSORING/MONITORING AGENCY NAME(S) AND ADDRESS(ES) Defense Threat Reduction Agency 8725 John J. Kingman Road Fort Belvoir, VA 22060-6201					10. SPONSOR/MONITOR'S ACRONYM(S) DTRA	
					11. SPONSOR/MONITOR'S REPORT NUMBER(S) DTRA-TR-16-66	
12. DISTRIBUTION/AVAILABILITY STATEMENT Distribution Statement A. Approved for public release; distribution is unlimited.						
13. SUPPLEMENTARY NOTES						
14. ABSTRACT Several techniques involving light filaments are investigated to achieve standoff detection of radioactive material decayed from a nuclear explosion. A new source is developed and produced high energy UV filaments. Theory shows the existence of coupled UV-IR filaments. Experiments demonstrate backward emission, to be exploited for standoff Raman detection. Stimulated Raman forward scattering of in air is observed with UV filaments. Combined UV and IR filaments lead to the demonstration of impulsive stimulated Raman scattering in the forward direction. Stimulated Raman Scattering in water is investigated, to understand the mechanism of backward emission, and means to enhance it.						
15. SUBJECT TERMS High power UV laser, Standoff Spectroscopy, nonlinear propagation in air, white light emission, polarization, Spatial heterodyne spectrometer, ultrafast video.						
16. SECURITY CLASSIFICATION OF:			17. LIMITATION OF ABSTRACT	18. NUMBER OF PAGES	19a. NAME OF RESPONSIBLE PERSON	
a. REPORT	b. ABSTRACT	c. THIS PAGE			Jean-Claude Diels	
U	U	U	U	39	19b. TELEPHONE NUMBER (Include area code) 505 272 7830	

## UNIT CONVERSION TABLE

U.S. customary units to and from international units of measurement<sup>\*</sup>

U.S. Customary Units	<div style="display: flex; align-items: center; justify-content: center;"> <div style="margin-right: 10px;"> </div> Multiply by </div> <div style="display: flex; align-items: center; justify-content: center;"> <div style="margin-right: 10px;"> </div> Divide by<sup>†</sup> </div>	International Units
<b>Length/Area/Volume</b>		
inch (in)	2.54 $\times 10^{-2}$	meter (m)
foot (ft)	3.048 $\times 10^{-1}$	meter (m)
yard (yd)	9.144 $\times 10^{-1}$	meter (m)
mile (mi, international)	1.609 344 $\times 10^3$	meter (m)
mile (nmi, nautical, U.S.)	1.852 $\times 10^3$	meter (m)
barn (b)	1 $\times 10^{-28}$	square meter (m <sup>2</sup> )
gallon (gal, U.S. liquid)	3.785 412 $\times 10^{-3}$	cubic meter (m <sup>3</sup> )
cubic foot (ft <sup>3</sup> )	2.831 685 $\times 10^{-2}$	cubic meter (m <sup>3</sup> )
<b>Mass/Density</b>		
pound (lb)	4.535 924 $\times 10^{-1}$	kilogram (kg)
unified atomic mass unit (amu)	1.660 539 $\times 10^{-27}$	kilogram (kg)
pound-mass per cubic foot (lb ft <sup>-3</sup> )	1.601 846 $\times 10^1$	kilogram per cubic meter (kg m <sup>-3</sup> )
pound-force (lbf avoirdupois)	4.448 222	newton (N)
<b>Energy/Work/Power</b>		
electron volt (eV)	1.602 177 $\times 10^{-19}$	joule (J)
erg	1 $\times 10^{-7}$	joule (J)
kiloton (kt) (TNT equivalent)	4.184 $\times 10^{12}$	joule (J)
British thermal unit (Btu) (thermochemical)	1.054 350 $\times 10^3$	joule (J)
foot-pound-force (ft lbf)	1.355 818	joule (J)
calorie (cal) (thermochemical)	4.184	joule (J)
<b>Pressure</b>		
atmosphere (atm)	1.013 250 $\times 10^5$	pascal (Pa)
pound force per square inch (psi)	6.984 757 $\times 10^3$	pascal (Pa)
<b>Temperature</b>		
degree Fahrenheit (°F)	$[T(^{\circ}\text{F}) - 32]/1.8$	degree Celsius (°C)
degree Fahrenheit (°F)	$[T(^{\circ}\text{F}) + 459.67]/1.8$	kelvin (K)
<b>Radiation</b>		
curie (Ci) [activity of radionuclides]	3.7 $\times 10^{10}$	per second (s <sup>-1</sup> ) [becquerel (Bq)]
roentgen (R) [air exposure]	2.579 760 $\times 10^{-4}$	coulomb per kilogram (C kg <sup>-1</sup> )
rad [absorbed dose]	1 $\times 10^{-2}$	joule per kilogram (J kg <sup>-1</sup> ) [gray (Gy)]
rem [equivalent and effective dose]	1 $\times 10^{-2}$	joule per kilogram (J kg <sup>-1</sup> ) [sievert (Sv)]

<sup>\*</sup> Specific details regarding the implementation of SI units may be viewed at <http://www.bipm.org/en/si/>.

<sup>†</sup> Multiply the U.S. customary unit by the factor to get the international unit. Divide the international unit by the factor to get the U.S. customary unit.



UV/IR filaments for high resolution novel spectroscopic  
Interrogation of Plumes on nuclear materials  
Final Report  
Basic Research Award # HDTRA1-11-1-0043  
Topic Per5-B  
The University of New Mexico

Dr. Diels, Jean-Claude, PI and Dr. Arissian, Ladan Co-Pi  
Adam Hecht, faculty  
The University of New Mexico,  
Center for High Technology Materials  
MSC 04-2710  
1313 Goddard SE  
Albuquerque, New Mexico 87106  
Phone 1 (505) 272 7830  
Fax 1 (505) 277 5843  
jcdiels@unm.edu

Matthias Lenzner, Subcontractor  
Lenzner Research

# Contents

<b>1</b>	<b>Abstract</b>	<b>3</b>
<b>2</b>	<b>Objective and relation to the DTRA mission</b>	<b>3</b>
2.1	Broad objectives . . . . .	3
2.2	Relation to the DTRA mission . . . . .	4
<b>3</b>	<b>Developments of a UV source for filaments</b>	<b>5</b>
3.1	Nd:YAG Oscillator Amplifier . . . . .	5
3.2	Pulse compression . . . . .	6
3.3	Recommendations for further improvement . . . . .	7
<b>4</b>	<b>Generation of UV filaments</b>	<b>9</b>
<b>5</b>	<b>Fundamental understanding of filaments</b>	<b>10</b>
5.1	UV filaments . . . . .	10
5.2	IR filaments . . . . .	10
5.3	Filament movies . . . . .	11
5.3.1	The Technique . . . . .	11
5.3.2	Time jitter elimination . . . . .	11
5.3.3	Solving longitudinal spatial jitter with the aerodynamic window . . . . .	12
5.3.4	Enhancing the Rayleigh scattering with aerosols . . . . .	13
5.4	Electronic polarization . . . . .	14
5.5	Molecular contribution to filamentation . . . . .	16
5.5.1	Effects of pre-filamentation propagation in air . . . . .	17
5.5.2	Evolution during the filament . . . . .	17
5.5.3	Intensity dependence of the rotation . . . . .	18
5.5.4	Post mortem: Change of ellipticity across the beam for in air . . . . .	20
5.5.5	Anomalous ellipticity and spectral broadening after the filament . . . . .	20
<b>6</b>	<b>Raman Scattering</b>	<b>21</b>
6.1	Stimulated Raman scattering with UV filaments . . . . .	22
6.2	Impulsive stimulated Raman scattering . . . . .	22
<b>7</b>	<b>Backward scattering</b>	<b>24</b>
7.1	Theory . . . . .	25
7.1.1	Stimulated Raman . . . . .	27
7.1.2	Impulsive Raman . . . . .	27
7.2	Experimental observation . . . . .	27
7.3	Stimulated Backward scattering in water . . . . .	28
7.3.1	Relevance . . . . .	29

<b>8</b>	<b>New high resolution/high throughput Spectrometer</b>	<b>30</b>
8.1	Overview . . . . .	30
8.2	Resolving power . . . . .	30
8.3	Technical details . . . . .	33
8.4	Resolution demonstration . . . . .	34

# 1 Abstract

In recent years, there has been a steady development of techniques to detect nuclear and radiological materials at standoff distances for nuclear nonproliferation and national security. These techniques include neutron detectors [1] and gamma-ray detectors [2] which require the production of highly energetic (MeV) electron beams, by large, heavy accelerators.

An investigation of several technique involving either a light filament, or a combination of light filaments, was made. The objective was to evaluate linear and nonlinear techniques that can be exploited for remote sensing with filaments. A long term objective was to obtain a remote signature of both the chemical composition and isotopic content of materials that result from the decay of radioactive materials involved in a nuclear explosion.

New diagnostic techniques were developed leading to a better understanding of filaments. These include influence of polarization, with either standard initial condition (beam focalization in air) or controlled initial condition (launching filaments from a focal spot in vacuum), developing a new video technique to visualize the evolution of the filamented pulse and plasma emission in time, space and frequency. Developments of a new source confirmed the creation of non diffracting ultraviolet “filament”, i.e. pulses of slightly less than 200 ps and 200 mJ energy, at 266 nm, confined to less than 1 mm diameter by nonlinear interaction with air, reported earlier [3].

Theoretical and experimental study were made of the combination of UV and IR filaments. The theory has shown the existence of stable steady state propagation of fs IR filaments coupled with UV filaments. Experiments have demonstrated backward emission, that can be exploited for standoff Raman detection. Stimulated Raman forward scattering of in air was observed with the UV filament alone. With a combination of UV and IR filaments, impulsive stimulated Raman scattering was generated in the forward direction. A study was made of stimulated Raman Scattering in water, in order to understand the mechanism of backward emission, and means to enhance it.

## 2 Objective and relation to the DTRA mission

### 2.1 Broad objectives

1. Understanding the physics and properties of high power filaments propagating in air, which include:
  - (a) Femtosecond IR (mJ) filaments
  - (b) Nanosecond UV (J) filaments
  - (b) A combination of both
2. Design means to extend the range over which such filaments can propagate
3. Study novel remote spectroscopic techniques exploiting the properties of filaments, including

- (a) Direct spectroscopy of particles dispersed in air
- (b) Spectroscopy of plume of material vaporized by the UV filament
- (c) Stimulated Backward Raman Spectroscopy of molecules

## 2.2 Relation to the DTRA mission

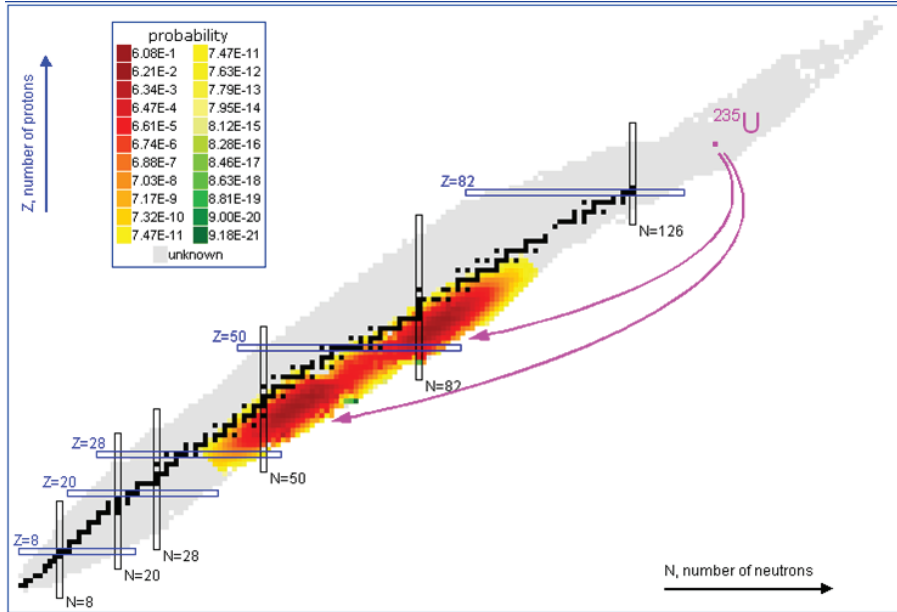


Figure 1: Distribution of fragments for the fission of  $^{235}\text{U}$ .

It is well known that, as a result of a fission reaction of a heavy nucleus, the fragments are distributed in two groups. These two groups can be seen in Fig. 1 which illustrates the distribution of fragments in the case of  $^{235}\text{U}$ . The higher mass distribution does not vary appreciably as a function of the mass of the parent nucleus or the energy of the neutrons involved in the reaction. The opposite can be said for the distribution of fragments centered at the lower average mass: a different distribution of lighter fragments is observed if the parent nucleus is  $^{235}\text{U}$ ,  $^{233}\text{U}$ ,  $^{239}\text{Pu}$ , or a mixture of those. Furthermore, the “gap” between the light and heavy distributions tends to fill up when higher energy neutrons are involved in the fission reaction. Each of the fragments has a larger number of neutrons than that corresponding to the most stable nuclei (black “stairs” curve in Fig. 1). They will evolve towards stability (horizontal line in the diagram) creating compounds of increasing stability, decreasing mass, and different chemical properties. The analysis of these compounds and their evolution in time should lead to a determination of the composition of the bomb that exploded.

The main questions that this program thrives to address are:

- Can these elements be identified by remote spectroscopy?
- Can *remotely* isotopic resolution of heavy elements be achieved?



- Can backward scattering be pumped by a narrow band UV filament, after being stimulated by an ultrashort pulse IR filament?
- Can isotopic selectivity be realized with Stimulated Backward Raman Scattering of molecules (oxides for instance)?

In Section 3, progresses in the development of a UV source for high energy filaments are reported. Evidence of UV filamentation is presented in Section 4. In parallel, a basic study of properties of IR filaments has been conducted. The goal is to contribute to a fundamental understanding of filamentation (Section 5).

## 3 Developments of a UV source for filaments

### 3.1 Nd:YAG Oscillator Amplifier

The original source of UV filaments (quadrupled Nd:YAG) has been upgraded by the addition of 2 amplifiers (to reach 7 J before frequency quadrupling) and by constructing a new feedback loop for seeding the Nd:YAG and have every pulse be single mode, longitudinal and transverse [4, 5]. Figure 2 shows a picture of the oscillator amplifier (right), and a block diagram of the various processes involved (left).

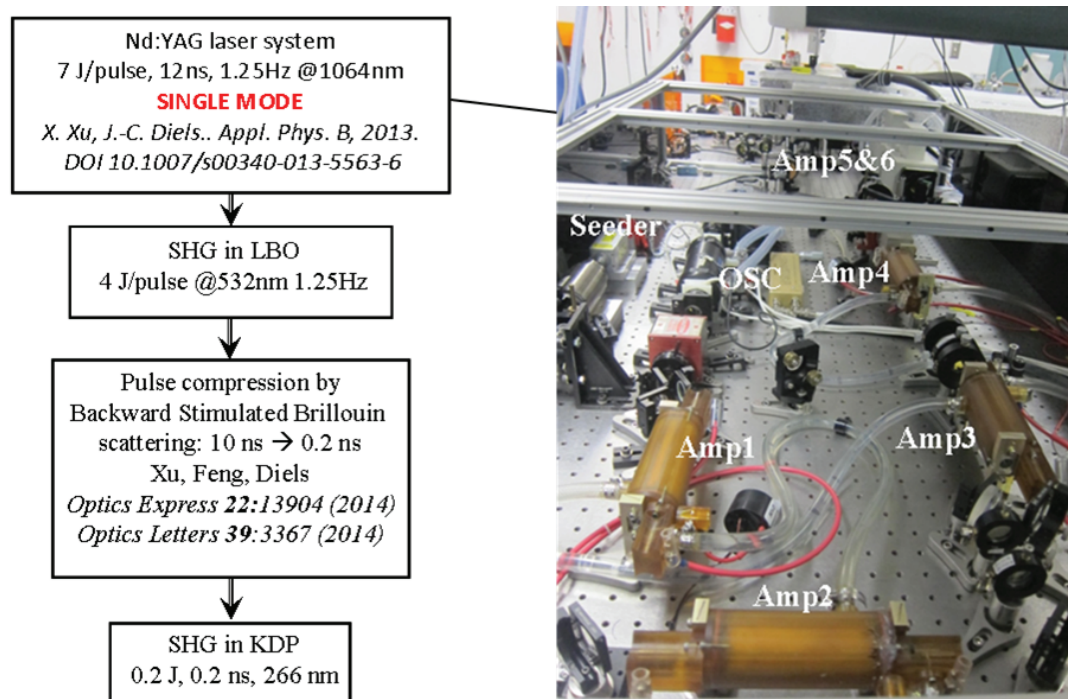


Figure 2: Left: block diagram of the various steps involved in the UV source. Right: picture of the Nd:YAG laser heads constituting the oscillator-amplifier.

The oscillator was originally designed with a very high output coupling, operating with very high gain, such as to produce extremely short Q-switched pulses (4 ns duration, corresponding to

barely 2 round-trips of the pulse in the cavity). In the original design, a seed laser was introduced in the resonator, with a feedback loop intended to force the YAG laser cavity to be resonant with the seed laser. The feedback loop was based on minimizing the build-up time of the Q-switched pulse. This system proved totally inadequate because (i) of the high losses of the laser cavity (poor mode identification with a cavity lifetime of only 2 round-trips) and the fact that the correction applied to the cavity is based on previous shots (a system totally inadequate in low repetition rate cavities). The solution was to operate the cavity at lower gain, higher Q, and stabilize the cavity *between* shots. The error signal is based on the reflection of the cavity to the seeder pulse, error signal that is interrupted by a mechanical shutter during the operation of the flashlamps. This system provided single mode operation at every shot. Its design and performances have been documented [4, 5, 6].

### 3.2 Pulse compression

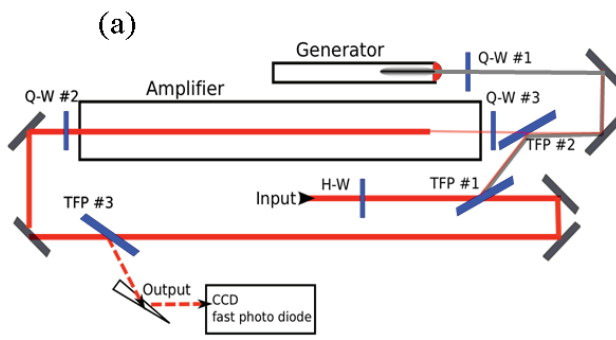
The re-designed 1064 nm system produces pulses of 9 ns instead of 4 ns. Therefore, pulse compression by stimulated Brillouin scattering had to be re-designed. A first improvement was to move from a single cell design to an oscillator–amplifier combination. The amplifier cell, adapted to the longer pulse duration, had to be 2.5 m long. The Brillouin scattering medium was fluorocarbon (FC72), selected by most researchers for its large Brillouin gain cross section. Theory and experiment showed that FC72 was not the best choice for high energy applications such as this one [7].

- There is a maximum pump *intensity* for reaching optimum conversion efficiency and compression. Already 10 cm aperture optics had to be used at the 1 J level in order not to exceed this optimum intensity with FC72
- The beams were continuously deflected through the cell, because of the large temperature dependence of the index of refraction  $dn/dT$ , and thermal gradients that could not be avoided despite best efforts to thermally isolate the liquid.

Our experimental and theoretical findings have been documented in [8, 6].

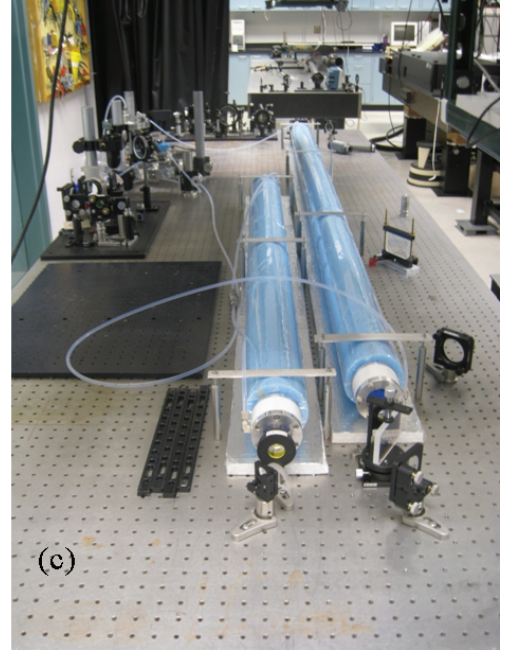
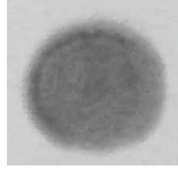
The solution to the problems cited above is to use a medium with *lower* Brillouin cross-section, and a smaller coefficient of index change with temperature. There are two candidates: water and heavy water. Both liquids have a smaller Brillouin cross section, and a zero  $dn/dT$ , at 4°C for water and 11°C. The difference is already significant at room temperature: for FC72,  $dn/dT = -4.7 \cdot 10^{-4} \text{ }^\circ\text{K}^{-1}$ , while for water,  $dn/dT = -0.8 \cdot 10^{-4} \text{ }^\circ\text{K}^{-1}$

For the 2.5 m long amplifier cell that has to be used, thermal convection remains a problem. The solution was to design a double walled water cooled cell, in which the windows were positioned *inside* the water cooled portion. Even this apparently perfect configuration did not allow us to operate at 4°C: at this temperature a thermal gradient appeared near the windows, resulting in non-uniform temperature, convection and beam deflection. Unlike the previous configuration with FC72, it was necessary to operate pulse compression at the second harmonic (532 nm) of the Nd:YAG wavelength, because of the absorption coefficient of water. This system however outperforms all other systems, in terms of energy (4J, only limited by the 5 cm cross section of the cell) and pulse duration (200 ps). Details on the system performances have been documented in references [9].



Amplified Brillouin @1.2J

(b)



(c)

Figure 3: (a) Schematics of the Brillouin compressor. A combination of half wave plate (HW) and thin film polarizer (TFP # 1) splits the input beam into a pump for the oscillator, and a pump for the amplifier. The stimulated backward Brillouin pulse generated in the oscillator (generator) returns with a polarization orthogonal to that of the pump, and is transmitted by the thin film polarizer TFP # 2 to enter as a seed into the amplifier cell. The circularly polarized seed pulse, counter-propagating to the main pump pulse in the amplifier cell, has its polarization rotated orthogonal to that of the main pump by the quarter wave plate QW # 2. The amplified/compressed seed pulse is extracted by the thin film polarizer TFP # 3. (b) show the beam profile of the output of the compressor. (c) is a view of the generator and amplifier cells in one layer of thermal isolation. More layers of isolation cover both tubes.

The compressed pulses were measured with a combination of fast detector/oscilloscope with a risetime of 200 ps. We used the recorded trace obtained with fs IR pulses as reference ( $\delta$ - function response). The convolution of the  $\delta$ - function response with the theoretical compressed pulse is compared in Fig. 4 with the measurement. The remarkable agreement indicate that our compressed pulse duration is not longer than 200 ps.

### 3.3 Recommendations for further improvement

It should be noted that slightly better performances should be obtained with heavy water, which has a zero  $dn/dT$  at 11°C, and a lower absorption coefficient at 532 nm. This was not attempted for budgetary reasons.

The spatio-temporal profile of the pulses from the Nd:YAG system before compression showed a lag of several ns between beam center and beam periphery. This will contribute to an elongation of a focused beam, since the periphery will trail the main pulse on axis by several ns [10]. This problem is present at the level of the oscillator and is well known from Nd:YAG laser manufacturers. It is an unavoidable by-product of the unstable resonator used for high power oscillators. As shown in Fig. 5, the pulse lag at the periphery is not affected by the seeding.

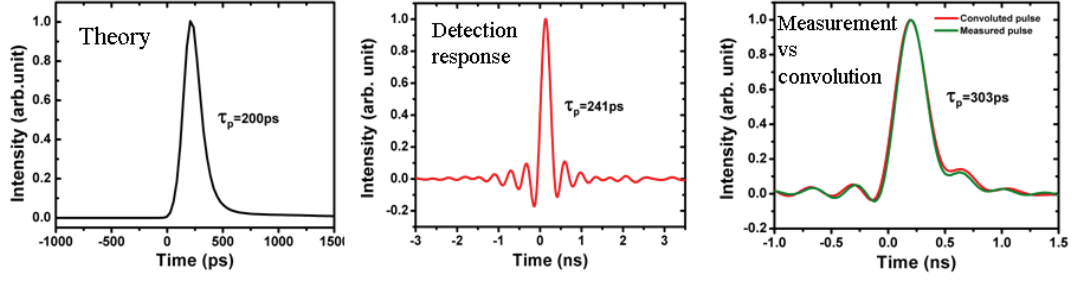


Figure 4: Left: the 200 ps pulse obtained from theoretical simulation of the compression by stimulated backward Brillouin scattering. Center: the  $\delta$ -function response of our detection system, obtained with a 50 fs at 800 nm. Right: the theoretical trace is convoluted with the impulse response, and compared with the measurement of the green compressed pulse.

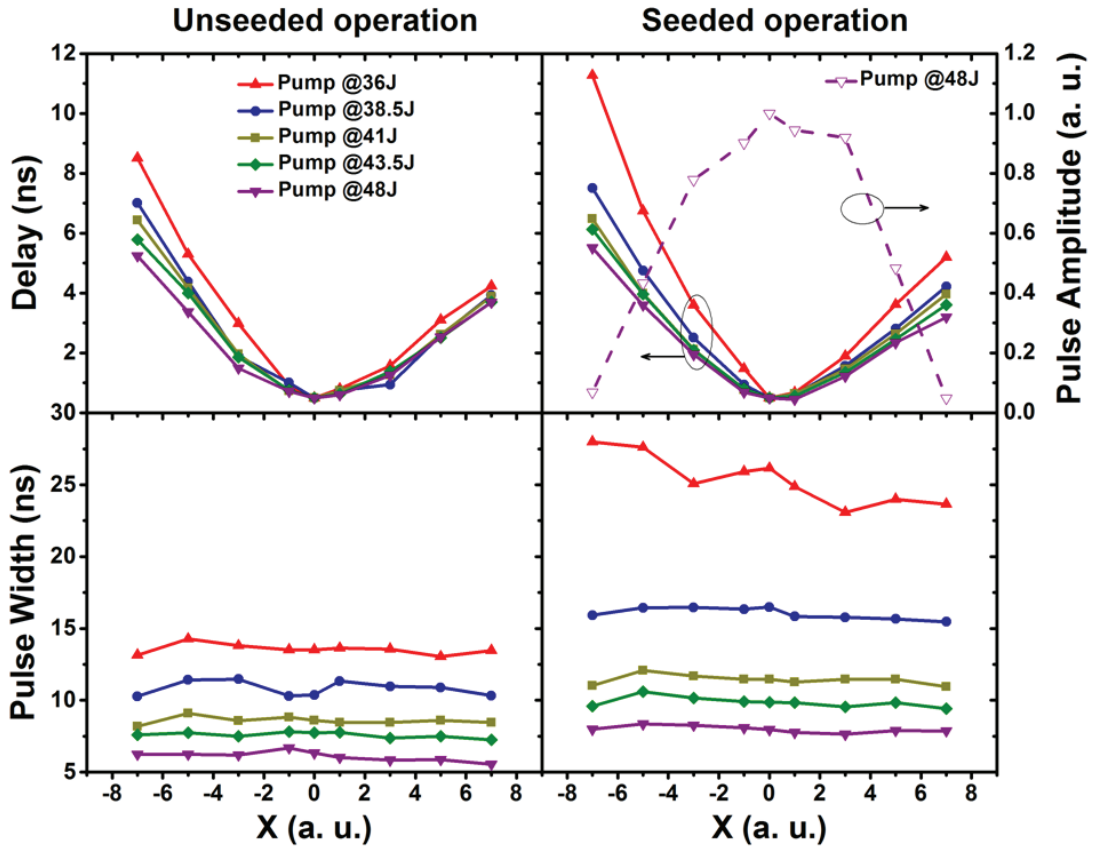


Figure 5: Timing of the leading edge of the oscillator pulse, and pulse duration, for various pump powers.

The solution is to use a stable Gaussian resonator at the oscillator. This solution was not implemented, because it requires one or two additional stages of amplification. The time lag of the periphery of the beam is reduced in the Brillouin cells.

## 4 Generation of UV filaments

Figure 6 demonstrate that the source described in the previous section is adequate to produce filaments in air. To ensure linear attenuation, the filaments were attenuated by a grazing incidence mirror, coated for maximum normal incidence reflectivity at 355 nm. We had shown previously that such a grazing incidence mirror is a linear attenuator, with a transmission factor of  $10^{-4}$  [11]. Top left figure shows a cross section through the profile taken by a CCD. The 2 cm diameter UV pulse is focused in vacuum, at the vacuum-air interface of an aerodynamic window [11]. Below critical power (13 MW), the radiation covers the full area of the CCD (the interference fringes that appear on the CCD are caused by neutral density filters used to attenuate the large beam. At higher power ( $\approx 500$  MW) a filament can be seen in the center of the CCD viewing area. The filament is seen to maintain its diameter after propagation through several meter (bottom).

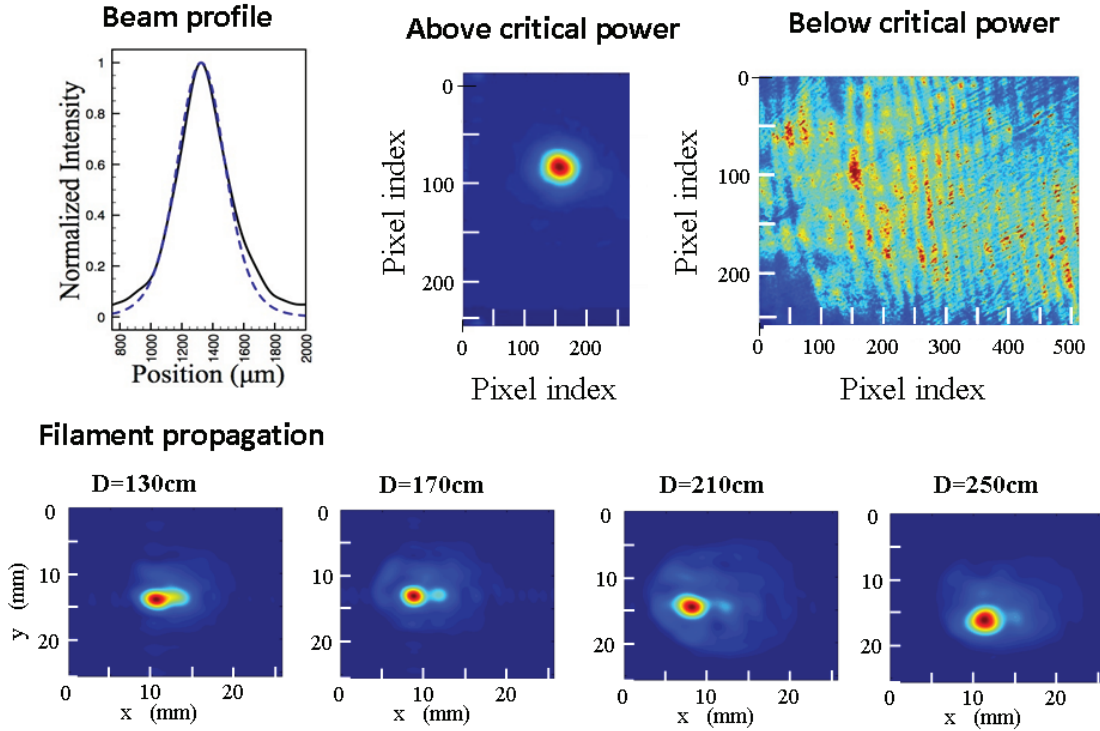


Figure 6: from top right to top left: beam profile recorded by the CCD camera at 1 m from the geometric focus, at low ( $\approx 1$  MW) power. The geometric focus is at the vacuum-air interface of an aerodynamic window. the beam profile is seen to fill the whole field of view of the CCD. Center: at 500 MW power, the beam has collapsed to a filament. Left: cross section through the profile showed in the center, and compared with the theory [3] (dashed line). Bottom, beam profile recorded at different distances from the aerodynamic window. The maximum distance was determined by the space available in the laboratory.



## 5 Fundamental understanding of filaments

### 5.1 UV filaments

Because of the higher nonlinearity in the UV, the intensity in the UV filament at 266 nm is two orders of magnitude smaller than in the IR filament. Because inverse Bremsstrahlung is considerably less effective in heating the electron plasma in the UV filament, considerably longer pulses (hundreds of picoseconds up to nanoseconds) of higher energy can be filamented. These facts simplify considerably the theoretical modeling, to the point that a simple quasi-steady state model has been appropriate in modeling the experimental observations [3].

The remainder of this section will address our contribution to the understanding of IR filaments.

### 5.2 IR filaments

Despite two decades of research, a fundamental understanding of filaments is still lacking. We have acquired a unique capability of launching filaments directly from a focused beam in air, through an aerodynamic window. The aerodynamic window was a key in the ability to realize ‘videos’ of the light bullet and the fluorescence and plasma radiation produced in its wake. Indeed, without the aerodynamic window, the starting point of the filament is not well defined, resulting in a loss of temporal resolution. The capability to control the initial condition prior to entering the atmosphere has enabled us to observe and analyze drastic differences between linearly and circularly polarized filaments, as well as made it possible to distinguish phenomena generated in the filament itself, from phenomena seeded in the preparation phase in air (i.e. during the self-focusing, prior to the formation of a filament). The picture is complicated by the entanglement of phenomena associated with electron motion, with a molecular contribution to the nonlinear index of refraction.

Some highlights of our studies and findings are:

- Movie of filaments showing the Rayleigh scattering trace of the beam, followed by delayed fluorescence of the molecules
- Electronic contribution to the nonlinear ‘index of refraction’: It cannot be simply described by a “Drude model” as has been done in most numerical simulations: the motion of electrons is neither isotropic nor harmonic [12].
- The properties of filaments are strongly dependent on the initial polarization.
- With initial elliptical polarization, there is a *rotation of the polarization ellipse* along the filament that can be attributed to the electronic nonlinear index [13], and be used as an independent measure of the focusing nonlinearity  $\Delta n_{NL} = n_2 I$ .
- There is a *change in ellipticity* that does not occur *during* filamentation but in the preparation phase in air (ellipticity change related to molecular orientation [13])
- There is a spectacular spectral broadening of the white light emission of filaments for a particular initial ellipticity, which exists only if the preparation phase is in air [14]

### 5.3 Filament movies

As mentioned above, the very nature of filamentation in air is still being debated. Questions still being asked are:

1. Is the filament a “moving focus” [15]?
2. Is the filament a "light bullet" propagating with a well defined group velocity [16]?
3. If it is a “light bullet”, is it expanding and contracting following what has been dubbed “Dynamic spatial replenishment” [17]?
4. Is the filament a “Bessel beam”, or does the nonlinear absorption influence the intensity profile as to produce self-focusing akin to axicon focusing [18]?

The distinction between these various models is not just academic. If the scenario (1) is correct, it would be impossible to have co-propagating filaments of different wavelength, and even have interacting filaments. The distinction between model (2) and (4) impacts the four wave mixing interaction that is an essential mechanism of coupling between filaments. In the model (4), the wave vectors cross the filament at a constant angle, while in the model (2), the wave vectors may be aligned on the filament axis, or as suggested by (3), change periodically along the filament. Providing a "movie" of the light intensity versus time, space and wavelength can resolve this controversy.

The results have been published in Journal of Physics B, special issue on filamentation [19]. Only a few main points are summarized here.

#### 5.3.1 The Technique

The horizontally propagating filament is imaged via two mirrors on the horizontally oriented slit of a streak camera, producing a 2D picture of intensity versus  $z$  and time, for a particular  $y$ . The  $y$  coordinate is varied by rotating one of the two mirrors about an horizontal axis. Images are continuously captured while the field of view is scanned along  $y$  by rotating a relay mirror, at a slow enough rate to ensure continuity in the longitudinal dimension. The individual images are then computationally organized by two dimensional ( $y, z$ ) pictures in successive time steps to provide a video. Over 1,000 synchronized frames of a streak camera are combined to produce the 4D (2 D space, time in ps and wavelength) movie.

#### 5.3.2 Time jitter elimination

In order to take advantage of the picosecond resolution of the streak camera in image reconstruction, the frames have to be synchronized accurately. There is 60 nanosecond delay between trigger and sweep of the streak camera. Therefore one can not use the same laser pulse to trigger the camera for the same frame. The streak camera is triggered electronically through the master clock of the laser system, thereby inheriting a 2ns jitter of the laser electronics. The accuracy of optical timing is transferred to each image by using a reference optical beam. A reference optical beam is selected from the same pulse that creates the filament and sent through a fixed path directly to the camera. The path of the reference beam is such as to illuminate always a point of the photocathode in the time frame of the camera streak, providing a temporal reference for every streak

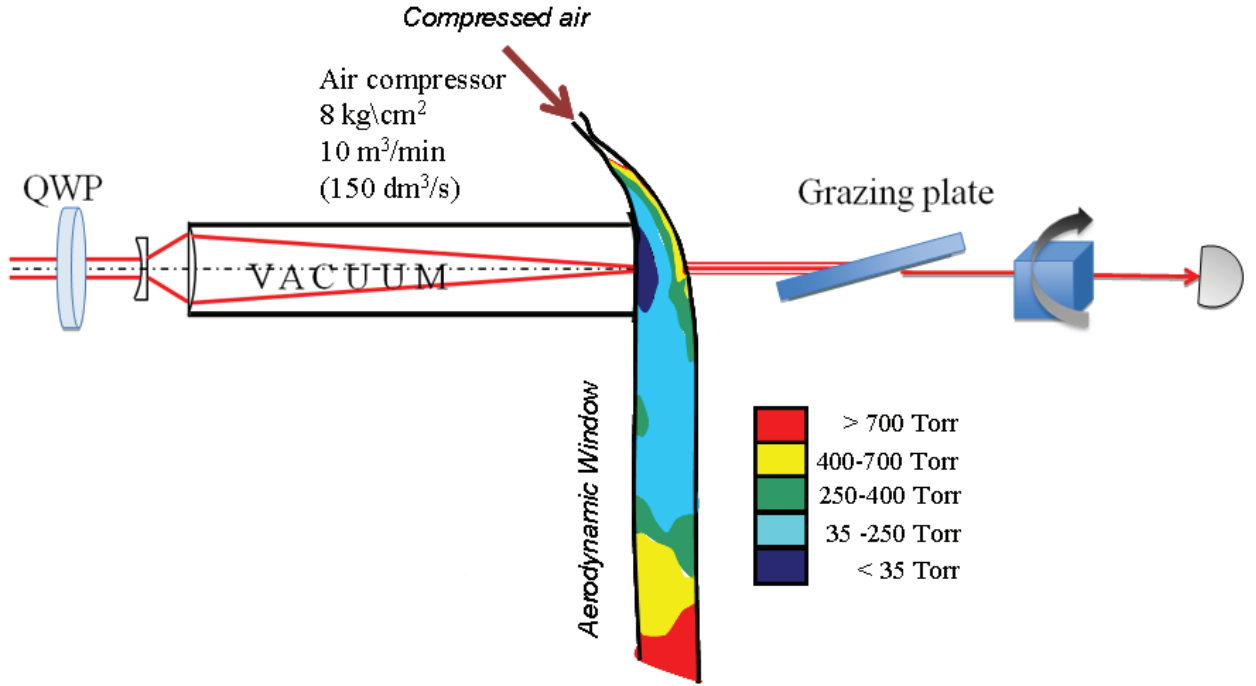


Figure 7: Experimental setup. The slit of a streak camera is located at the image plane of the object (the filament). The light is relayed via a periscope made of two large UV enhanced aluminum mirrors, one of which can be rotated. In the arrangement of the figure, the slit of the camera is parallel to the propagation axis  $z$  of the filament. With the streak camera being triggered when the filamented pulse is in the field of view of the camera, the frame displays light intensity versus time and  $z$  (a line along the filament). The real image of the filament is moved from shot to shot across the slit with rotating mirror. The angle is scanned over 6 mrad in 400s, time during which 1,300 frames (or more) are recorded. Each frame contains the space time information along a line along the filament.

camera image. Since each filament is a single shot study, the optical reference provides the timing of the event, and absolute timing is not needed. Mechanical and electronic jitter between frames are corrected by using the timing of the reference pulse in the reconstruction code. Successive ( $y$ ,  $z$ ) frames are stitched together with the accuracy of the streak camera. The reference beam can not be used with closed commercial camera objectives. In those images the optical reference in the frame is a reflection of a fixed element in the imaging scene.

### 5.3.3 Solving longitudinal spatial jitter with the aerodynamic window

*a) focusing in air* Tight focusing creates a brighter plasma and a shorter filament. Filaments are typically launched with lenses of longer focal length, about 3 m with their intensity “clamped” at  $3 \cdot 10^{13} \text{ W/cm}^2$ . One such typical filaments is presented in Fig. 8 (a) for focusing in air. The intensity averaged in a 100 pixelx100 pixel around the middle of the filamentation region was selected to generate a plot of radiated intensity versus time [Fig. 8 (b)]. It show a plasma risetime of 90 ps and a fall time of 200 ps.

#### *b) Focusing in vacuum*

The length of the trace representing the plasma in Fig. 8 may not be representative of the true

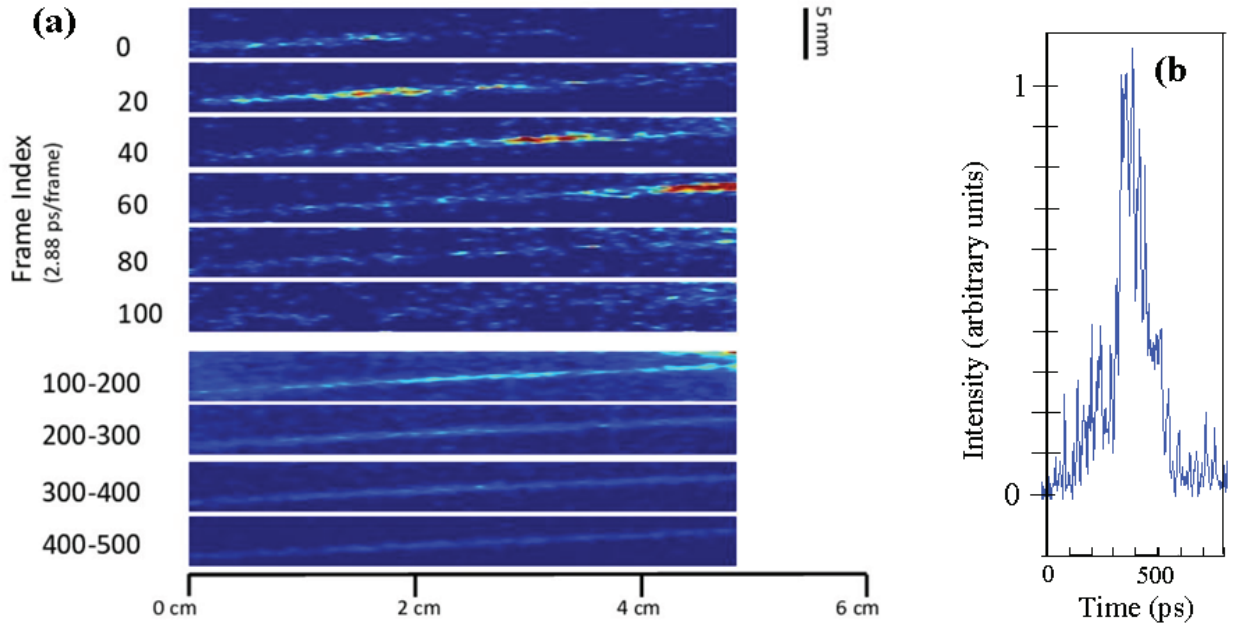


Figure 8: (a) Filament of a 800nm pulse using long focal length in air with unfiltered detection. Frames are separated by 2.88 ps. Selected frames are shown between frame 1 to 100. For later frames an average over 100 frames is shown to reduce noise. (b) Intensity of the radiation versus time. The intensity is averaged over 50x50 pixels around the position  $z = 2$  cm.

plasma length if there is a jitter in the starting point of the filament (along  $z$ ). To ensure that the starting point of filaments in air is repeatable, the pulses are focused in vacuum onto the 2 mm transition region vacuum-atmosphere of an aerodynamic window [11]. In this configuration the filament is created at the exit of the window in atmospheric air. Using this method the shot to shot generation of plasma and filament is well aligned in the three dimensional space. Selected frames are shown in Fig. 9 (a). The emission is indeed shorter (along  $z$ ) and brighter. The plasma emission is plotted in Fig. 9 (b). The reduced jitter enables a much better resolution of the 40 ps rise time and 230 ps fall time (both times being measured from 10% to 90%).

### 5.3.4 Enhancing the Rayleigh scattering with aerosols

To enhance the image brightness we use a method to create water droplets for increased scattering. The aerosols are blown through the camera field of view along the path of the filament in the opposite direction of the propagation of the pulse. Aerosols have their own (slow) nonlinearity as they migrate towards the center of a beam, a nonlinearity that has made it possible to observe filamentation in liquids with mW cw powers [20]. It has been reported that aerosols ( about 15  $\mu\text{m}$  radius) influence the collapse position of the filament [21]. This should not be a factor in the present experiment, since the filaments were prepared in vacuum, and the aerosols stop at the vacuum-air boundary. It is known that large water droplets can interrupt filamentation, which then is recreated from the surrounding filament reservoir [22]. This is however a major perturbation of the filaments itself, and defeats the purpose of observing an unperturbed filament. Attempts with different sources of aerosols (for instance ultrasound fog generators) failed because of the bright

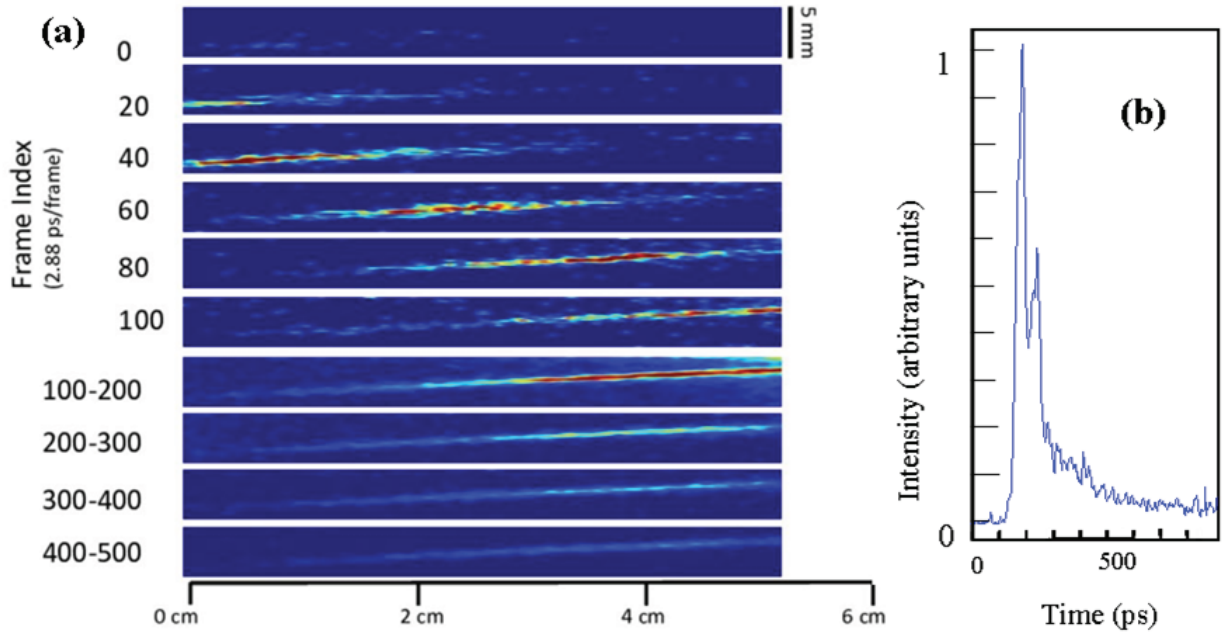


Figure 9: Filament of a 800nm pulse with unfiltered detection, focused with 3 meter focal length lens in vacuum through an aerodynamic window. Selected frames are presented from frame 1 to 100. For longer times an average over 100 frames is shown to reduce noise. (b) Intensity of the radiation versus time. The intensity is averaged over 50x50 pixels around the position  $z = 2$  cm.

plasma generated by the droplets [23]. Large droplets create also enhanced scattering through optical (whispering gallery modes) resonances [24]. The solution chosen is to produce droplets of 1 to 5  $\mu\text{m}$  diameter with a nebulizer (mist generator based on Bernoulli principle). These droplets were sufficiently small as not to create any visible plasma or local illumination. Selected frames from the video are shown in Fig. 10 (a). The video shows a short lived pulse propagating from left to right which we interpret as Rayleigh scattering from the laser pulse, followed by some plasma emission from the water droplets. The observed peak has a FWHM of 85 ps [Fig. 10 (b)].

## 5.4 Electronic polarization

Measurements with the aerodynamic window (focusing in vacuum) have proved the inadequacy of the Drude model used nearly universally to explain the index of refraction of the electrons created by multiphoton ionization (or tunneling) in a filament. The wrong assumptions are (i) to assume an isotropic distribution of electrons, and (ii) a uniform distribution of electrons close to equilibrium. These assumptions only hold after a time laps of 1 ps, and not in the femtosecond time scale of the pulse. In a general case the motion of the electrons may not be a harmonic oscillator motion, or it could be driven by multiple electric fields. In the case of gases weakly ionized by ultra-short pulses, the electrons that follow the laser field are neither bound nor free. These considerations led to a review paper, presenting a simple approach to calculate the electron index based on a known electron motion in a non-relativistic regime [12]. In this paper, the electron index is calculated as a radiation response of charges in an infinitesimal cross section of the beam. Typical of filamentation conditions in air with IR pulses, the laser pulse length is short enough to neglect electron-electron



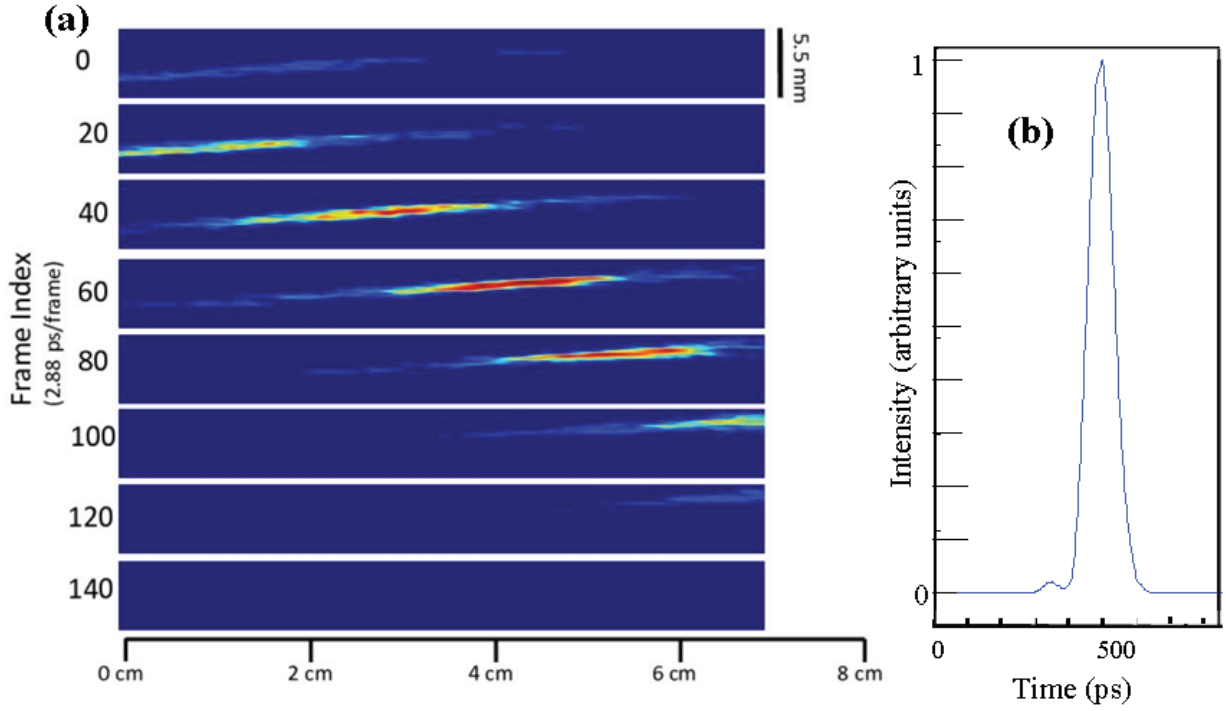


Figure 10: Portion of the filament propagating through dense water vapor. Rayleigh scattering is increased due to micron sized water droplets.

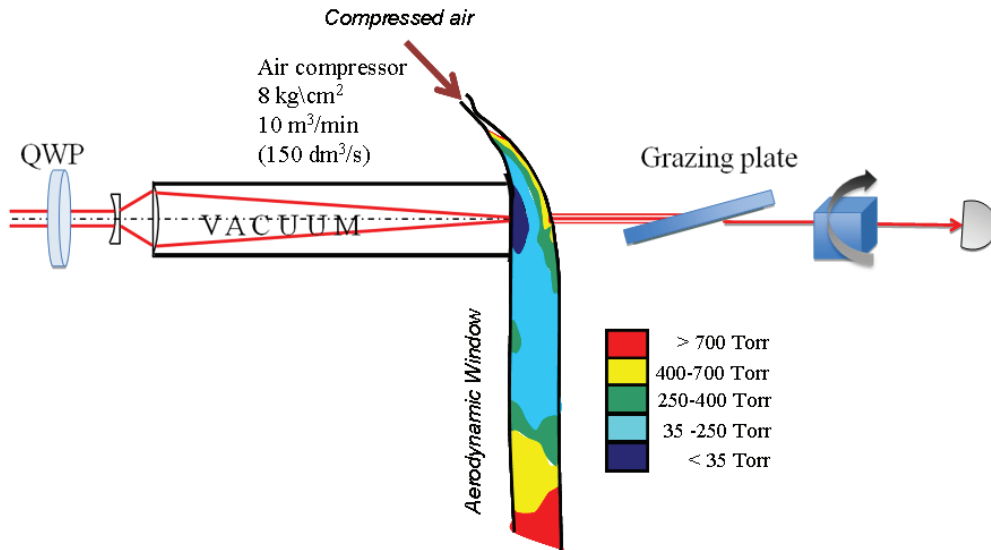


Figure 11: The laser beam is sent through a quarter wave plate to prepare the polarization, and focused by a telescope into a 3 m long vacuum cell sealed by an aerodynamic window. Measurements are presented either with the cell evacuated or at atmospheric pressure. The polarization measurement includes a 1 mm thick grazing incidence plate for linear attenuation of the beam, and a rotating cube polarizer to record the polarization ellipse. Because of the size of the grazing incidence plate, measurements labeled “at focus” are in fact 4 cm beyond the estimated focal point.

collisions and the ion's motion. The laser pulse is long enough to neglect influences of carrier to envelope offsets (the change in peak field is small from one oscillation to the next). We refer to the publication [12] for more details.

## 5.5 Molecular contribution to filamentation

The change of light polarization before and after the formation of a filament has been explored. Detailed measurement of polarization evolution of 60 fs, 800 nm light pulses as a function of prepared light ellipticity were made. A major conclusion is that the polarization of the filament is in general unpredictable, unless the beam has been pre-focused in vacuum [25, 11]. This is not only an academic question, but important in numerous applications which are polarization dependent, such as THz generation. Another example is interacting filaments, or coupled solitons, where one filament serves as a waveguide to another. The intensity and length of the generated plasma is dependent on the particular state of polarization, and whether this polarization is maintained along the filament. This applies to remote sensing applications in general, where the signals from a distant target are created by the filament and the forward [26, 27] or backward [28] signal is collected. In these cases a thorough understanding of spatio-temporal properties of the propagating light is of great interest [29] as it affects the signal [i.e. light induced breakdown spectroscopy (LIBS) or Raman].

A sketch of the measurement setup is presented in Fig. 11. The state of polarization is measured along the filament, as function of the initial polarization. The polarization state of the laser is modified by a quarter wave plate (QWP) positioned after the source, and rotated by increments of a few degrees. To avoid nonlinear effects at the detection, a grazing plate attenuates the beam, prior to a complete measurement of the polarization ellipse using a rotating polarizing cube.

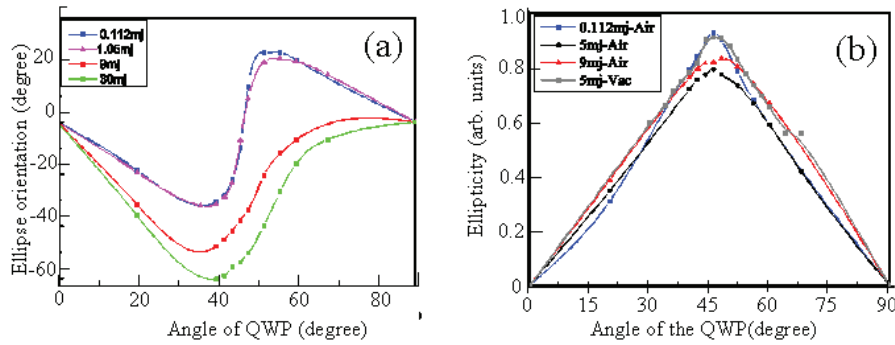


Figure 12: a) Rotation of the polarization ellipse as a function of QWP angle at different pulse energies, for a 60 fs beam propagating in air, measured at the starting point of the filament. The ellipse angle rotates with change of the input pulse energy. b) Measurement of light ellipticity at the filament starting point, with increase of input pulse energy. The average retardation angle for the filament spectral width is only  $87^\circ$  instead of  $90^\circ$ , which explains that the ellipticity does not reach one, at 45 degree of QWP angle, for the lowest input energy of 0.112 mJ. The change of ellipticity is more pronounced around  $45^\circ$  and polarization becomes more linear as the energy is increased. At higher energies (above 5 mJ) the contribution of peripheral beam has to be considered. The shape of the ellipse does not undergo a visible change for focusing in vacuum.

### 5.5.1 Effects of pre-filamentation propagation in air

Figure 12 clearly shows that the polarization ellipse of the beam is modified at the starting point of the filament. Figure 12 (a) (left) shows the rotation of the ellipse as a function of pulse energy, recorded at the start of the filament. While obvious, it is verified by measurements on the filament just after its creation through focusing in vacuum and transmission through an aerodynamic window, that such a rotation does not take place.

More striking is the change in ellipticity, defined as the ratio of the minor axis to major axis of the ellipse. Figure 12 (b) shows that, near circular polarization, the ellipticity is modified at the starting point of filaments focused in air, a modification that does not take place, as expected, in the case of filaments prepared from vacuum.

### 5.5.2 Evolution during the filament

The polarization rotates at a constant angle during the filament, independently of the initial energy. This is illustrated in Fig. 13, which shows approximately the same rotation of the polarization ellipse for different initial pulse energies. This confirms the existence of a “clamping intensity”. The measurement of the rotation provides a new, independent method of determining the product of the clamping intensity times the nonlinear index  $n_{2B}I$ , where  $n_{2B}$  is the value of the nonlinear index that contributes to rotation, and that includes a small electronic component and a large molecular (rotational) component. This coefficient is different from the one responsible for self-focusing.

To clarify the distinction, some nonlinear optics formulae are reproduced below.

For non-resonant interactions, the nonlinear polarization can be written [30]

$$P = \epsilon_0 6\chi_{1122}(E \cdot E^*)E + 3\epsilon_0 \chi_{1221}(E \cdot E)E^* = \epsilon_0 A(E \cdot E^*)E + \frac{1}{2}\epsilon_0 B(E \cdot E)E^*. \quad (1)$$

Coefficients “A” and “B” are related to nonlinear susceptibilities through  $A = 6\chi_{1122}$  and  $B = 6\chi_{1221}$ , and  $\epsilon_0$  is the vacuum permittivity. For molecular alignment  $B = 6A$ ; for electronic Kerr effect  $B = A$ , and  $B = 0$  for electrostriction effect. Only the coefficient  $B$  is responsible for polarization rotation. If we use circular polarization as a basis,

$$E_{\pm} = \frac{E_x \pm iE_y}{\sqrt{2}}, \quad (2)$$

where  $E_+$  and  $E_-$  are the right and left circular components. The polarization (1) can be written in these basis as:

$$P_{\pm} = \epsilon_0 A|E_{\pm}|^2 E_{\pm} + \epsilon_0 (A + B)|E_{\mp}|^2 E_{\pm}^*, \quad (3)$$

Using the wave equation for plane wave propagation, the nonlinear polarization leads to the following change in index:

$$n_{\pm} \simeq n_0 + \frac{1}{n_0} [A|E_{\pm}|^2 + (A + B)|E_{\mp}|^2]. \quad (4)$$

The total induced birefringence is thus:

$$\Delta n = n_+ - n_- = \frac{B}{2n_0} (|E_+|^2 - |E_-|^2) = n_{2B}I, \quad (5)$$

which leads, for a filament of length  $\ell$ , leads to the rotation:

$$\theta = \frac{1}{2} \Delta n k \ell. \quad (6)$$

The nonlinear index responsible for self-focusing and determining the clamping intensity is given by Eq. (4), while the index responsible for rotation is given by Eq. (5).

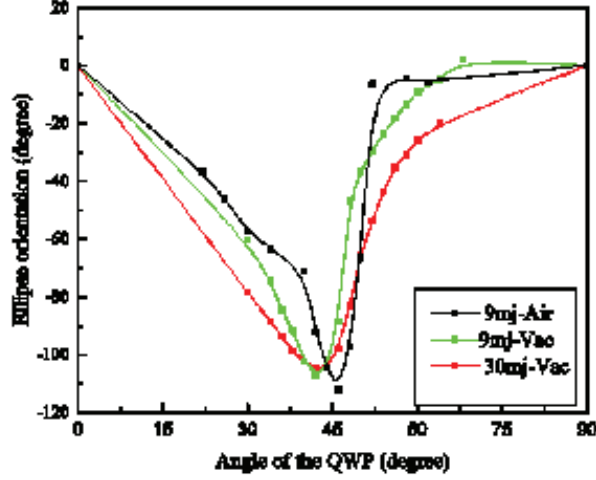


Figure 13: Rotation of polarization after 61 cm of filament propagation, for a pulse energy of 9 mJ, prepared in air and vacuum, and energy of 30 mJ, prepared in vacuum. The polarization does not change its orientation after the beam diverges.

### 5.5.3 Intensity dependence of the rotation

The rotation of polarization, as pointed out above, is intensity dependent. Therefore, different spectral components, dependent on their intensity, are expected to show a different ellipse rotation. In order to test this point, the beam issued from the filament is spectrally separated by a pair of prisms. The polarization ellipse is analyzed for three different parts of the spectrum, shown in Fig. 14 (a). For each of the three parts of the spectrum, a different rotation is observed [Fig. 14 (b)]. As expected, the component centered at 795 nm is the most intense and shows the largest rotation (black curve), while the component centered at the longest wavelength (820nm) experience a small rotation of its ellipse. These data are taken for a 60 fs pulse, 9 mJ energy, 167 cm after the filament created by 3 m focusing in vacuum (and launched in the atmosphere through the aerodynamic window). With this type of preparation, there is little broadening of the initial pulse spectrum, in contrast to the white light emission generated by filaments prepared in air.

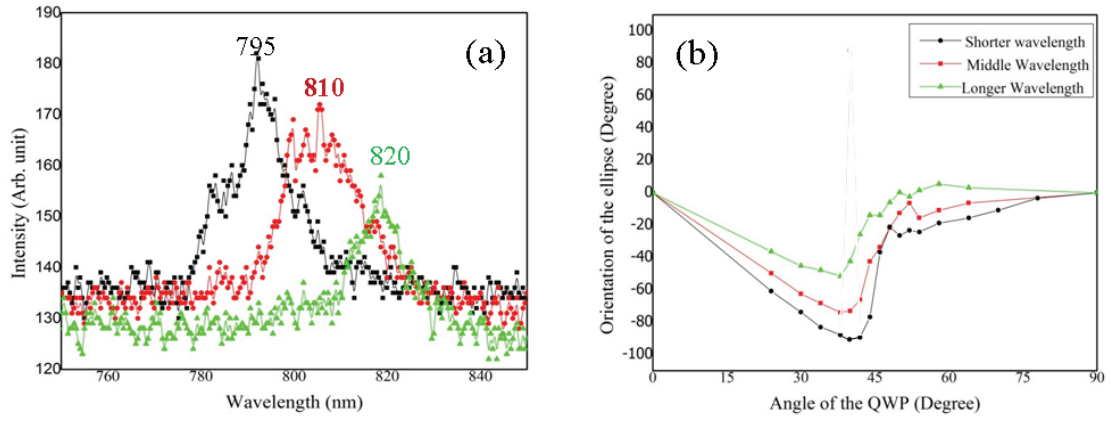


Figure 14: Ellipse rotation versus intensity/wavelength. Data taken 167 cm after the filament prepared in vacuum with a 60 fs pulse. (a) Decomposition of the pulse spectrum in 3 components by a pair of prisms. (b) Rotation of the polarization ellipse, measured for each of the spectral component shown in (a).

### 5.5.4 Post mortem: Change of ellipticity across the beam for in air

It is remarkable that the filaments characteristics are still very much affected by the initial propagation in air *after* the filament has dissipated. This is illustrated by the plots of Fig. 15. It is again observed that very little ellipticity change or structure is observed for filaments prepared in vacuum (Fig. 15 left). The center of the beam having a slightly larger intensity, one can expect larger nonlinear absorption of the major axis of the ellipse, which explains the observed increase in ellipticity (Fig. 15 left). In addition, we observe no visible conical emission. By contrast, there are significant ellipticity changes, which depend on the radial position, in the case of filaments prepared in air (Fig. 15 right).

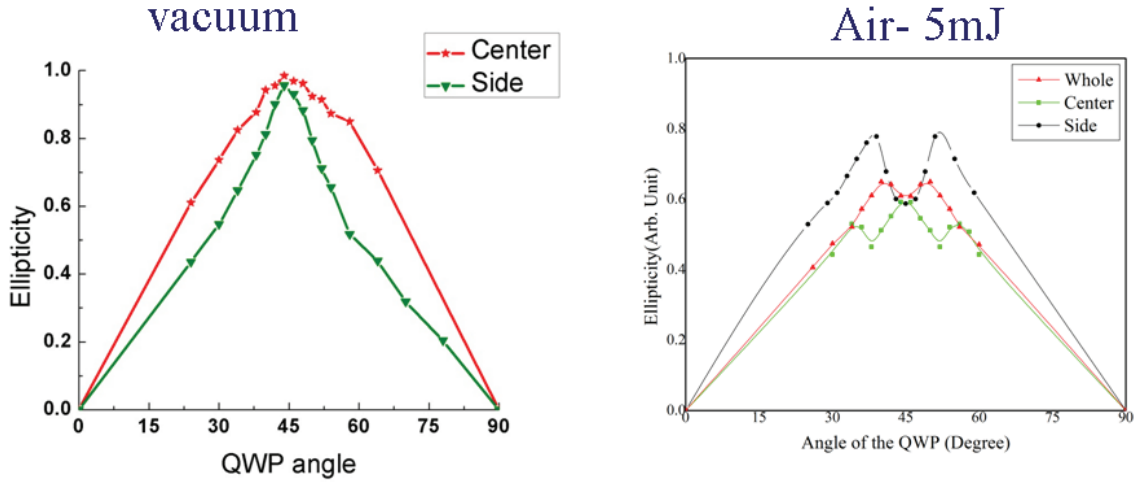


Figure 15: Change of ellipticity across the beam for preparation in vacuum and air. Left: preparation in vacuum: no ellipticity structure is observed for focusing in vacuum. In addition, conical emission is not visible for filament prepared in vacuum. Right: important ellipticity modifications are observed close to the initial circular polarization, observed only for preparation in air.

### 5.5.5 Anomalous ellipticity and spectral broadening after the filament

Systematic spectral recording were made of the white light emission after filaments, as a function of the ellipticity. This work was performed in collaboration with a group of the University of Central Florida [14]. Only for filaments prepared in air, and for specific *initial* ellipticity (close to circular), the white light spectrum is seen to extend to the blue. This effect is correlated with a change in ellipticity, and is not seen for filaments prepared from vacuum. Figure 16 (a) shows the spectrum versus ellipticity in the case of nitrogen at 0.7 atm. The large spectral extension is seen for the angle of the quarter wave plate placed after the laser source of 39° and 51°. The filament length is also extended for this particular initial ellipticity (not shown in the figure). A picture of the beam after the filament shows clearly the change in color at these specific angles [Fig. 16 (b)]. This effect is associated with a decrease in ellipticity at the same angle of the quarter wave plate [Fig. 16 (c)]. If the filament is prepared from a focal spot in vacuum [Fig. 16 (c)], there neither a change in ellipticity, nor a spectral broadening towards the blue. These effects are seen in all

molecular gases, but not in rare gases. This indicates that re-orientation of the molecules plays a role, in qualitative agreement with computer simulations [14].

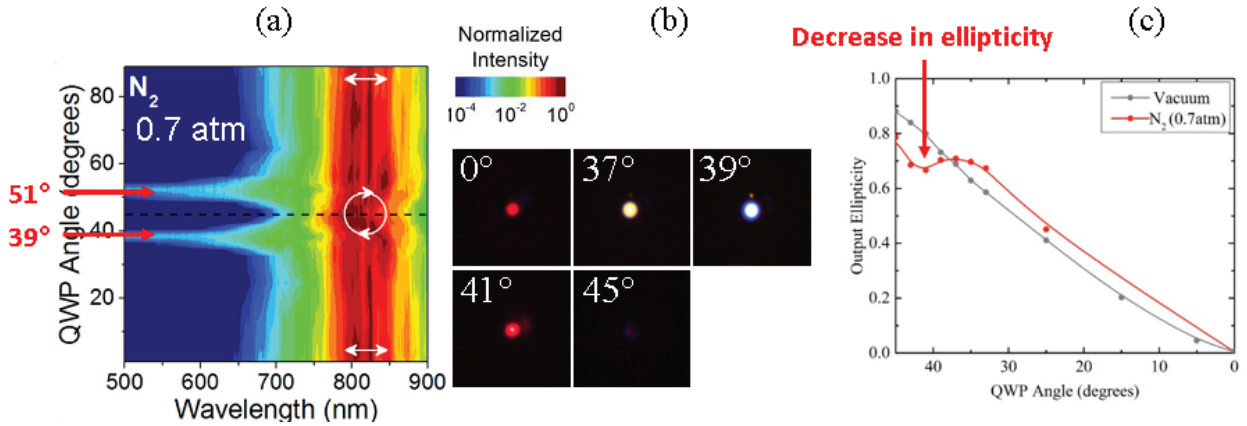


Figure 16: Post filament characteristics (approximately 1 m after the dissipation of the filament) prepared in air as a function of initial ellipticity of the laser beam. The ellipticity is varied from linear to circular to linear with a quarter wave plate placed after the laser source. The data are given as a function of the angle of the quarter wave plate. The measurements are made in nitrogen at 0.7 atm. (a) White light spectra recorded as a function of the angle of the quarter wave plate. An large extension of the spectra towards the blue is observed for quarter wave angles of 39° and 51°. (b) Photographs of the filament show that at these angle, the color of the filament can be seen to change towards the blue. (c) The ellipticity measured at the same location as the spectra (i.e. after the filament) does not follow the ellipticity of the initial beam, but has an anomalous decrease at 39° (red curve). The blue curve shows that the ellipticity to be that of the initial beam for filaments prepared in vacuum.

## 6 Raman Scattering

Since the UV filament is made with a bandwidth limited (1 GHz) pulse, it is an ideal pump for Raman scattering.

The objective was to demonstrate a new method of remote stimulated Raman spectroscopy of plumes created by a laser filament. The molecules to be detected are excited by the short pulse IR pulse, while the co-propagating UV pulse (200 ps) provides stimulated Raman scattering of the excited sample. The successive steps are:

1. Co-propagating UV and IR filaments?
2. Demonstrating stimulated Raman scattering with UV filaments
3. Study of selective Impulsive Raman scattering with combined IR and Uv filaments
4. Finding optimal conditions for Backward stimulated Raman scattering.

The first point has been the subject of a theoretical investigation in collaboration with the group of Professor Aceves at Southern Methodist University in Dallas [31]. The surprising result is that, both in the non-resonant case ( the coupling is mainly the result of the nonlinear index) and the



resonant case (the UV photon is just equal to 3 IR photons, and the coupling is dominated by four wave mixing), there are "coupled solution" solutions by which the two beams are propagating inside each other [31]. This result implies that for experiments calling for simultaneous radiation in the IR and UV, only one of the two laser needs to be filament producing. This is an interesting mathematical problem of coupled solitons, in which the two-color filaments (UV and IR) preserve similar scaling properties of the Townes soliton and that they co-exist as one component (UV) guiding the other (IR). In all cases, numerical propagation produced quasi-stable behavior over extended distances. It is expected that these properties make them a more natural state for long lived filaments, one likely easier to realize experimentally. The UV component being 3 orders of magnitude longer than the fs IR, group velocity mismatch plays no role. For long range detection, there is benefit of carrying energy in two distinct frequencies and distinct energy range. The front and back of the quasi-CW UV pulse modifies the ionization state of the propagating medium felt by the IR pulse. The presence of a long robust UV pulse will favor a more stable IR filament as it will not only transversally confine the IR filament, but it partially ionize the front and the back of the channel where the IR pulse propagates. Details of this theoretical investigation can be found in reference [31].

## 6.1 Stimulated Raman scattering with UV filaments

Filament induced Raman scattering can be used for remote detection of molecules and molecular fragments. The spontaneous Raman scattering is however too weak to be of any use in remote sensing. With sufficient intensity, there is sufficient gain for a strong Stokes or antistokes Raman line to be observed. Stimulated Raman scattering for vibrational spectroscopy of gas samples has been demonstrated in IR filaments [32], using the fs pulse of the filament (800 nm) to vibrationally excite the components of air, and a stretched second harmonic pulse (400 nm, 1 ps) as the Raman pump. The THz bandwidth of the probe limits the resolution of this method. In the case of solid targets, the use of UV filaments has two advantages over the technique of ref. [32]. With an energy close to 1 J, a UV single filament creates a denser ablation plasma than a single mJ IR filament. The 266 nm UV laser source produces 200 ps that are bandwidth limited ( $\Delta\nu \approx 2$  GHz) and are therefore an ideal Raman pump signal. This 2 GHz represent a considerably better resolution than the THz pulse at 400 nm.

The experimental setup consists in the UV source creating a filament. In the path of the filament, grazing incidence plates are used as attenuators. The attenuated radiation is sent into a 1 meter spectrometer. Stimulated forward Raman scattering is seen clearly in Fig. 17 With a pulse energy of  $\approx 300$  mJ, sharp lines corresponding to stimulated (vibrational) Raman lines of nitrogen are seen in Fig. 17. One unexpected feature is a very large antistokes to Stokes ratio, which seems to indicate that the filament has created an inversion in the vibrational ladder. The ratio of antistokes to Stokes intensity decreases with intensity. A 20 mJ focused UV beam creates lines of nearly equal intensity.

## 6.2 Impulsive stimulated Raman scattering

Figure 17 showed Raman emission from Nitrogen clearly spectrally resolved from the UV radiation of the filament. This stimulated Raman emission has a considerably lower threshold if the molecule is put in vibration by other means. A fs IR filament is used to excite molecules in the

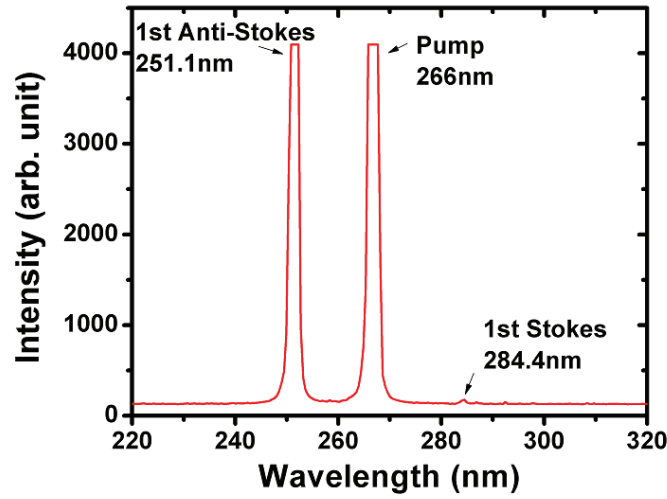


Figure 17: Stimulated (forward) Raman emission of nitrogen in a UV filament. Note the huge contrast between the antistokes and Stokes component. Both the antistokes and the pump saturate the detector.

path of the filament. A co-propagating UV filament (narrow band) serves as pump for stimulated Raman scattering. This spectroscopic technique is of considerable range, and many orders of magnitude more sensitive than spontaneous Raman scattering. Because of the small difference of refractive index between 266 nm and 800 nm ( $24 \cdot 10^{-6}$ ), a fs IR filament and a 200 ps UV filament will co-propagate for approximately 2 km.

The measurements are performed with the experimental setup sketched in Fig. 18. The fs IR beam and the ps UV beam are combined via a beam splitter. The leakage of 800 nm radiation through a turning mirror is frequency doubled to 400 nm, and sent onto a fast vacuum photodiode simultaneously with the radiation at 266 nm, in order to record the exact delay between the IR impulse and the UV Raman pump. The two lasers are synchronized electronically. There is however a ns jitter inherent to the Q-switch seeding process [4]. The timing between pulses is monitored by a fast UV vacuum photodiode, which is detecting the UV beam and the second harmonic of the IR pulse. Several grazing incidence plates are used to attenuate the beam, before it is sent to a spectrometer.

In order to ensure that the signal is due to excitation of the molecules rather than being the stimulated Raman seen in Fig. 17, only weak UV radiation ( $< 20$  mJ) is used. Theory (cf. Section Raman theory) has shown that the excitation pulses have to be shorter than the period of the oscillation to be observed. The 50 fs pulses from the present laser are longer than the period of vibration of nitrogen. It is however adequate to excite rotational lines in oxygen and nitrogen. Figure 19 (a) shows the rotational spectrum recorded in the forward direction. Note that the UV radiation is sufficiently narrow band so that there is not measurable scattering from the 266 nm laser at the two data points on either side of the laser line. The energy scan 19 (b) shows a clear threshold for this nonlinear process. The two curves at 267.3 nm and 264.8 nm are recorded in the same condition. At the energy level of 20 mJ used for the UV, we have not observed a dependence on the UV power. Figure 19 (c) is a plot of the Raman signal dependence on the delay between the near-IR impulse and the UV Raman probe.

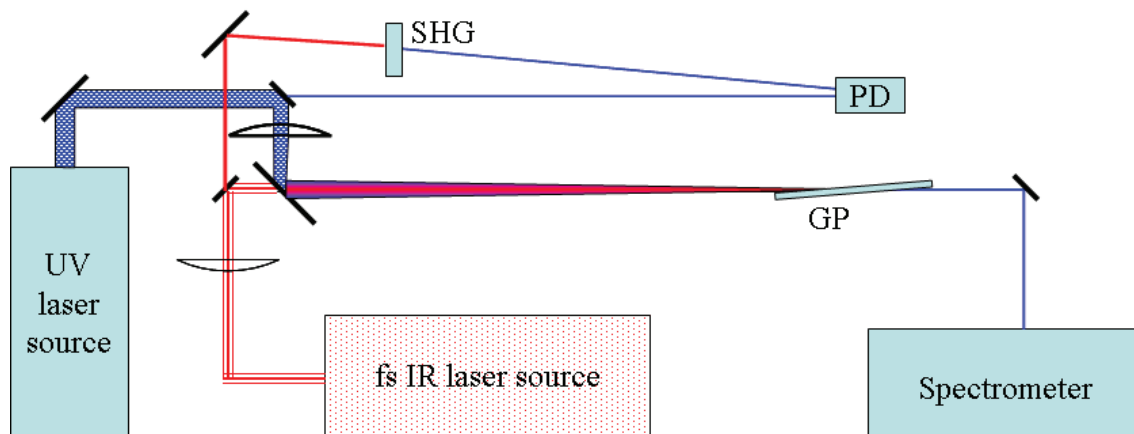


Figure 18: Setup for impulsive rotational Raman scattering. A dichroic beam splitter is used to combine the UV and IR beams, which are focused by 3 m focal distance lenses to create the filament. The second harmonic of the leakage through the IR turning mirror is sent on a UV fast vacuum photodiode, together with the leakage of the 266 nm turning prism. The photodiode records the delay between the two pulses with a resolution of 200 ps. The radiation from the filament is attenuated by grazing incidence plates before being sent to the spectrometer.

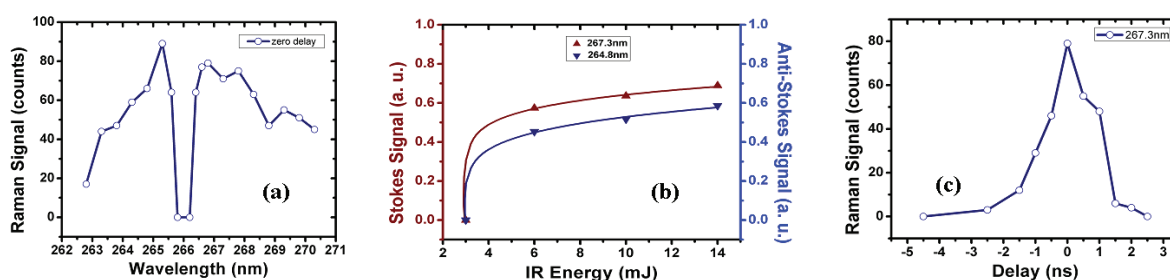


Figure 19: (a) Impulsive Rotational Raman spectrum of nitrogen. In this case, the anti-Stokes and Stokes components are of the same order of magnitude. (b) Dependence of the Stokes and anti-Stokes signals on the infra-red intensity. (c) Dependence of the signal on the relative delay between near- IR and UV.

Impulsive stimulated Raman scattering through excitation with ultrashort pulses is particularly promising for remote detection. One particular advantage that remains to be researched is the possibility to put the molecular selectivity in the excitation. Indeed, instead of  $\delta$ -function excitation of the rotation or vibration of a molecule, one can use a sequence of pulses matching a particular vibration, or use spectrally shaped pulses. The selectivity is thus put on the emission rather than on the detection.

## 7 Backward scattering

Backward stimulated Raman spectroscopy has been developed since the 60's [6]. Impulsive stimulated Raman scattering is a technique that uses pulses shorter than the duration of vibration periods to create a vibrational excitation that will be subsequently amplified by a Raman pump [7]. In a first application to the study of air with filaments, the vibrational excitation was produced by the

broadened spectrum in the 800 nm pulse of the filament, and the Raman pump by the second harmonic of that pulse [8]. However, the short duration of the Raman pump implies a very short gain length in the backward direction, hence precludes the possibility of stimulated backward scattering. The broad spectrum of the short pulse used also limits the spectral resolution. Our approach is to use the narrow bandwidth of the UV (filamented) pulse as Raman pump. The gain length for backward stimulated Raman is two to three orders of magnitude larger than in the experiment of Odhner et al. [8].

## 7.1 Theory

With the elastic collision time of molecules in the atmosphere being of the order of 100 ps, we are clearly in the regime of coherent interaction. We have therefore established a system of equations for coherent Raman excitation and propagation based on a simple three level system. Multiphoton transition are the result the combination of all allowed dipole transitions in the system. Each of the off-resonant dipole transition can be treated adiabatically.

We are considering here three optical frequencies: the Raman pump  $\omega_{\ell,1}$ , the Stokes  $\omega_{\ell,2}$  and the antistokes  $\omega_{\ell,3}$ . The subscript  $\ell$  is there to remind that we are talking about light frequencies and not atomic level frequencies. The levels are labeled 0 for the ground state, 2 for the Raman level ( $0 \rightarrow 2$  is dipole forbidden) and 1 for any level of the atom/molecule connected by dipole transition to 0 and 2. Rather than carry around sum symbols, we will assume there is a level 1 closer to “resonance” than all other ones. The three level system equations will be reducing to two levels by making the approximation that level 1 is far off resonance with any other level coupled by any of the light fields (that will be the adiabatic approach). For the Raman case of interest, only resonant Raman makes sense, meaning that the difference between the pump and the Raman radiation is always equal to the vibration frequency being excited  $\omega_{20}$ . We consider  $\omega_0$  and  $\omega_2$  referring the lowest states and  $\omega_1$  to the upper state. Our derivation includes simultaneously the pump, Stokes and antistokes field, so that the system is excited by the tri-chromatic field:

$$E(t) = \mathcal{E}_1(t) \cos[\omega_{\ell,1}t + \varphi_1(t)] + \mathcal{E}_2(t) \cos[\omega_{\ell,2}t + \varphi_2(t)] + \mathcal{E}_3(t) \cos[\omega_{\ell,3}t + \varphi_3(t)]. \quad (7)$$

Using the Hamiltonian of dipole interaction, the time evolution of eigenvalue of each state “k” is

$$\frac{da_k}{dt} = -i\omega_{0k}a_k + \sum_j \frac{i}{2\hbar} p_{kj} [\tilde{\mathcal{E}}_p e^{i\omega_p t} + \tilde{\mathcal{E}}_s e^{i\omega_s t} + \tilde{\mathcal{E}}_{as} e^{i\omega_{as} t} + c.c.] a_j. \quad (8)$$

In which  $p_{kj}$  is the transition strength between levels “k” and “j” and  $p_{kj} = p_{jk}$ . The fields and de-tunings are defined as

$$\begin{aligned} \delta &= \omega_2 - \omega_0 \\ \Delta &= \omega_p - \omega_{10} \\ \tilde{\mathcal{E}}_u &= [\tilde{\mathcal{E}}_p e^{i\omega_p t} + \tilde{\mathcal{E}}_s e^{i\omega_s t} + \tilde{\mathcal{E}}_{as} e^{i\omega_{as} t}] e^{-i\omega_p t} \\ &= \tilde{\mathcal{E}}_p + \tilde{\mathcal{E}}_s e^{-i\delta t} + \tilde{\mathcal{E}}_{as} e^{i\delta t} \end{aligned} \quad (9)$$

This is the rotating wave approximation with rotation at pump frequency  $\omega_p$ , replacing “a” eigen-

values with “c”s

$$\begin{aligned} a_0 &= c_0 \\ a_1 &= c_1 e^{-i\omega_p t} \\ a_2 &= e^{-i(\omega_{as}-\omega_p)t} c_2 = e^{-i\delta t} c_2 \end{aligned} \quad (10)$$

in which

$$\begin{aligned} \frac{da_0}{dt} &= \frac{dc_0}{dt} \\ \frac{da_1}{dt} &= -i\omega_p a_1 + e^{-i\omega_p t} \frac{dc_1}{dt} \\ \frac{da_2}{dt} &= -i\delta a_2 + e^{-i\delta t} \frac{dc_2}{dt} \end{aligned} \quad (11)$$

Substituting in equation (8)

$$\begin{aligned} \frac{dc_0}{dt} &= i\kappa_{01} E_u c_1 \\ \frac{dc_1}{dt} &= -i\Delta c_1 + i\kappa_{01} c_0 E_u^* + i\kappa_{12} c_2 E_u^* e^{-i\delta t} \\ \frac{dc_2}{dt} &= i\kappa_{12} c_1 E_u e^{i\delta t} \end{aligned} \quad (12)$$

In which  $\kappa_{ij} = \frac{p_{ij}}{2\hbar}$ . Considering the fact that level “1” is far off resonant we can implement the condition for the steady state of level “1”  $dc_1/dt = 0$  which results into

$$c_1 = \frac{1}{\Delta} (\kappa_{10} c_0 E_u^* + \kappa_{12} c_2 E_u^* e^{-i\delta t}) \quad (13)$$

To simplify the notations, we use:

$$\begin{aligned} \tilde{\mathcal{E}}_a &= \frac{p_{10}}{2\hbar\sqrt{\Delta}} E_u \\ \tilde{\mathcal{E}}_b &= \frac{p_{12}}{2\hbar\sqrt{\Delta}} E_u \end{aligned}$$

$$\begin{aligned} \frac{dc_0}{dt} &= i|\tilde{\mathcal{E}}_a|^2 c_0 + i\tilde{\mathcal{E}}_a \tilde{\mathcal{E}}_b^* e^{-i\delta t} c_2 \\ \frac{dc_2}{dt} &= i\tilde{\mathcal{E}}^* \tilde{\mathcal{E}}_b e^{i\delta t} c_0 + i|\tilde{\mathcal{E}}_b|^2 c_2 \end{aligned} \quad (14)$$

The three level problem is reduced to a two level problem, where “Q” and “W” are pseudo vectors forming a Bloch sphere.

$$\begin{aligned} \rho_{20} &= c_0 c_2^* \\ \rho_{22} - \rho_{00} &= c_2 c_2^* - c_0 c_0^* = W \\ \frac{d\rho_{20}}{dt} &= \dot{c}_0 c_2^* + c_0 \dot{c}_2^* \end{aligned} \quad (15)$$

Substituting, after some manipulations, we find the reduced equations:

$$\begin{aligned}
\dot{\tilde{Q}} &= -i \left[ |\tilde{\mathcal{E}}_b|^2 - |\tilde{\mathcal{E}}_a|^2 - \delta \right] \tilde{Q} + 2\tilde{\mathcal{E}}_a \tilde{\mathcal{E}}_b^* W - \frac{\tilde{Q}}{T_2} \\
\dot{W} &= - \left[ \tilde{\mathcal{E}}_a \tilde{\mathcal{E}}_b^* \tilde{Q}^* + \tilde{\mathcal{E}}_a^* \tilde{\mathcal{E}}_b \tilde{Q} \right].
\end{aligned} \tag{16}$$

We can generally assume that  $p_{10} = p_{12}$ , implying that  $\tilde{\mathcal{E}}_a = \tilde{\mathcal{E}}_b = \tilde{\mathcal{E}}_u$ . The propagation equations are

$$\begin{aligned}
\frac{\partial \tilde{\mathcal{E}}_p}{\partial z} + \frac{1}{c} \frac{\partial \tilde{\mathcal{E}}_p}{\partial t} &= -\alpha_p (Q \tilde{\mathcal{E}}_s + Q^* \tilde{\mathcal{E}}_{as}) \\
\frac{\partial \tilde{\mathcal{E}}_s}{\partial z} + \frac{1}{c} \frac{\partial \tilde{\mathcal{E}}_s}{\partial t} &= -\alpha_s Q^* \tilde{\mathcal{E}}_p \\
\frac{\partial \tilde{\mathcal{E}}_{as}}{\partial z} + \frac{1}{c} \frac{\partial \tilde{\mathcal{E}}_{as}}{\partial t} &= -\alpha_{as} Q \tilde{\mathcal{E}}_p
\end{aligned} \tag{17}$$

### 7.1.1 Stimulated Raman

In the case of stimulated Raman, the initial conditions are that  $\tilde{\mathcal{E}}_s = \tilde{\mathcal{E}}_{as} = 0$ . The Raman signal has to evolve from noise., unless a seed is introduced for the Stokes or antistokes field.

### 7.1.2 Impulsive Raman

In this case we have the very short 800 nm fs pulse of which the spectrum is broader than  $\omega_2 - \omega_0$ , and  $\tilde{\mathcal{E}}_1 = \tilde{\mathcal{E}}_2 = \tilde{\mathcal{E}}$ . We have a forward propagating wave  $E = \tilde{\mathcal{E}} e^{i(\omega t - kz)}$ , creating the Raman excitation  $\tilde{Q}$  with no spatial harmonic dependence. It is often assumed that a sufficient condition for creating the Raman excitation  $\tilde{Q}$  is that the *spectrum* of the exciting field covers the Raman frequency  $\omega_{20}$ . The form of Eq. (\*7.1) show that this is incorrect, because the driving term  $\tilde{\mathcal{E}} \tilde{\mathcal{E}}^*$  is proportional to the pulse *intensity*, independent of the pulse phase or phase modulation. Pulse durations of the order of 25 fs have thus to be used for impulse excitation of the vibration of simple diatomics such as nitrogen.

## 7.2 Experimental observation

Backward radiation could be detected from UV filaments, as demonstrated by Fig. 20. In these preliminary data, no attempt to spectral resolution was made. The UV beam was focused through a hole in a parabolic mirror, before producing a filament. The backward emitted signal that does not fall through the hole is focused onto a fast vacuum photodiode. Figure 20 (a) shows the return from the beam dump, as well as a peak corresponding to the radiation scattered on the side of the hole in the parabolic mirror.

In Fig. 20 (b) a 266 nm reflector at 45° incidence attenuates by a factor of 20 all radiation around 266 nm. The trace shows time of arrival of scattered radiation. The 266 nm beam is scattered by the edges of the hole producing a small peak indicated by a white arrow at the beginning of the trace. The white oval indicates backward radiation that corresponds to region indicated by a red oval in the sketch. Finally, a third peak corresponds to the radiation scattered by the beam dump situated at the end of the room. These results show it is possible to detect backwards scattered

radiation with this optical arrangement and could be adapted to detection of emission lines with spectral filtering and resolution. The approach taken here has the advantage that the maximum of UV energy is sent out to the atmosphere, but only the portion of the backscattering that is not exactly backscattered is detected. A relatively insensitive photodiode was used in order to identify through time of flight the origin of the detected signal. Ultimately, spectral resolution is needed, which can be combined with some temporal resolution by using a gated image intensifier.

Further attempts have to be made to spectrally resolve the radiation. Experiments described in the next section suggest that it is most likely Brillouin scattering. However, the presence of the filter should have considerably attenuated this component.

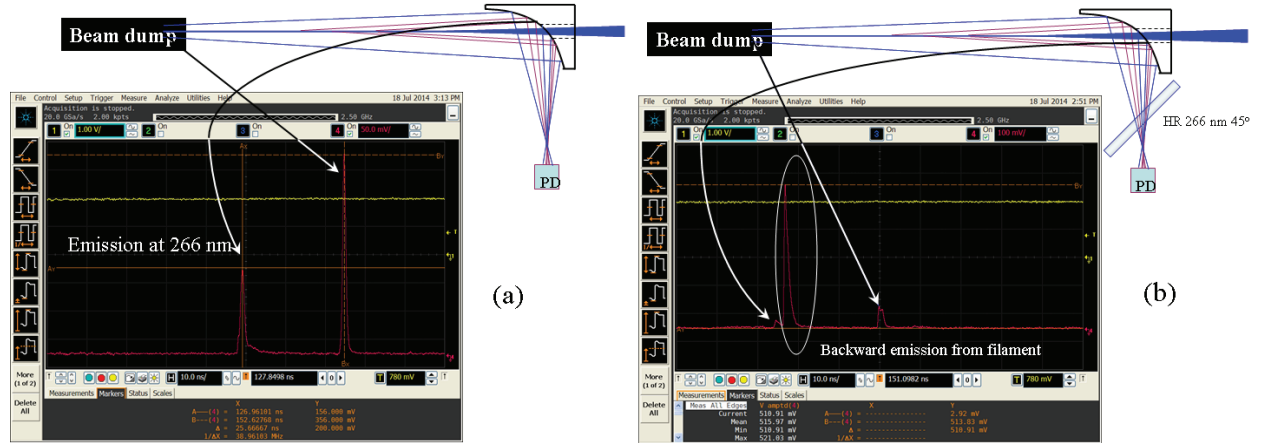


Figure 20: (a) Top: sketch of the experimental arrangement. The beam is focused through the hole in an off-axis parabolic mirror. A fast vacuum photodiode detects the backscattered radiation. The oscilloscope trace shows a return from the side of the UV beam scattering at the edges of the hole in the parabolic mirror. A second pulse is the backscattering from the beam dump. (b) A high reflector at 45° incidence mirror has been added to attenuate the 266 nm radiation. Both backscattered signals seen in (a) are seen to be strongly attenuated. A stronger backscattered signal originates from the location where the region of highest intensity in air.

### 7.3 Stimulated Backward scattering in water

Because of the difficulties in spectrally and temporally resolving the backward radiation in air, experiments were conducted at 532 nm in water, where Raman returns are more readily observable. The questions that these experiments were to address are:

1. What is the polarization dependence of backward Raman scattering?
2. What is the pulsewidth dependence of backward Raman scattering?
3. What is the impact of filamentation on the ratio of backward to forward Raman?
4. What is the physical origin/content of the backward radiation?

The experiment consists in focusing pre-compressed pulses ( $\approx 532$  nm, 200 ps) from a single-cell stimulated Brillouin scattering pulse compressor in a water cell. Forward and backward radiations are spectrally resolved. The maximum energy efficiency of 9% achieved by employing a



circularly-polarized pump pulse. The backward emission is strongly pulsewidth dependent, increasing with increasing pulsewidth. As the pump pulse energy increases, the ratio of backward to forward decreases. Backward radiation is larger than forward at low energies and for circular polarization. This particular point is illustrated in Fig. 21 (a), where the stimulated Raman energy is plotted as a function of pump energy in both backward and forward directions. It is interesting to note that the decrease in backward and increase in forward emission coincide with the onset of filamentation, and correlates with a drastic change in standard deviation of the data [Fig. 21 (b)].

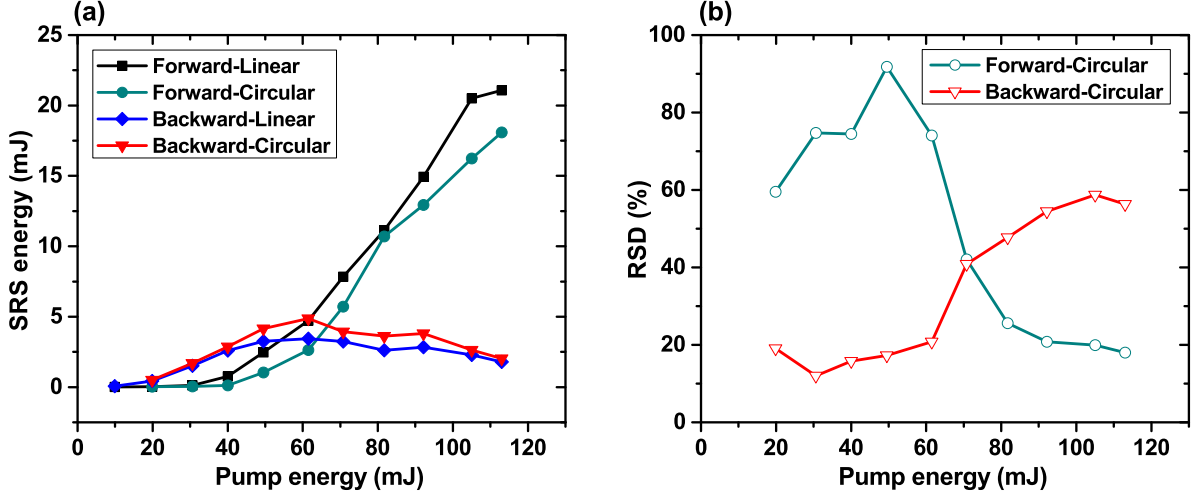


Figure 21: (a) SRS output energies at both linear and circular pump polarization; (b) Relative Standard Deviation (RSD) of SRS energy at circular pump polarization. Forward and backward denote the SRS propagation direction with respect to the pump; Linear and circular refer to the pump polarization.

The somewhat surprising result of the study, details of which can be found in reference [33], is that the stimulated backward Raman results for forward Raman of the stimulated backward Brillouin scattering.

### 7.3.1 Relevance

Simple back of the envelope calculation of the Brillouin gain in air indicate that substantial Brillouin scattering should be observed (which could be the peak observed in Fig. 20 (b)). These experiments indicate also that circular polarization should be used. The pulsewidth dependence calls for using nanosecond pulses of higher energy, rather than 200 ps. This is in fact to be expected: the gain length for the backward radiation is only the pulse length, or roughly 6 cm, while the forward gain length extends for the whole length of the filament. Similar observations have been made with IR filaments. Direct backward Raman emission is never observed. When Raman radiation is observed in the backward direction of the filament, it is generally forward Raman from inversion lasing in the backward direction.

In order to perform Raman spectroscopy in the backward direction, it appears that a strong pump beam has to be generated by another mechanism in the backward direction. This problem should be re-evaluated in light of previous observation made of backward emission. There has been few studies [34, 28] on the backward emission of IR filaments. It has been shown [28] that the supercontinuum emission from a filament is enhanced in the backward direction compared

with linear backscattering. This enhancement was interpreted as being due to a backscattering process in laser-induced longitudinal refractive-index changes caused by Kerr and plasma effects. Subsequent study by the same group [34] showed that the LIBs emission to be enhanced in the backward direction by aerosols. This effect, attributed to nonlinear interaction within the aerosol, would impact Stimulated Backward Raman Scattering, as it provides a seed for the amplified emission towards the source.

## 8 New high resolution/high throughput Spectrometer

### 8.1 Overview

The challenge optical identification of isotopes is resolution, and high throughput. The isotope shift that must be measured/detected is directionally proportional to the difference in the atomic mass unit (a.m.u.) of the isotopes. It has been reported that the isotope shift for uranium U-238/235 using the U(II) line at 424.347 nm is  $+1.39 \text{ cm}^{-1}$  (or 0.025 nm) with a linewidth of  $0.67 \text{ cm}^{-1}$  (0.012 nm) [35]. We are therefore aiming for a resolution of 0.006 nm or better.

The initial proposed approach was to use the spatial heterodyne spectrometer designed for astronomy [36]. This device is basically a Michelson interferometer in which the two mirrors have been replaced by gratings in first order of diffraction. The gratings are imaged on a CCD camera, which records an interferogram, the Fourier transform of which is the spectrum to be measured. the following shortcomings of this instrument have been identified.

1. The expression derived in the literature for the resolution of this instrument are only valid for radiation of infinite coherence (i.e. lines of zero width), a situation totally unrealistic
2. While fringes can easily be seen in zero order (implying zero resolution), the alignment is extremely tedious and only feasible with laser sources
3. The bandwidth is limited by the spatial resolution of the detector arrangement, since the further away a spectral component is from the Littrow wavelength, the higher the spatial frequency of the Fizeau fringe pattern that it generates.

Item (2) has been solved by variations of the arrangement sketched in Fig. 22. Mounting the two gratings back to back on a common rotation stage eliminates the problem of synchronizing their Littrow angles. Also, this configuration mitigates the angular alignment (horizontal and vertical) of the two arms, since not the two gratings mounted on the rotation stage but only the two more stably mounted mirrors have to be aligned. Items (1) and (3) require some compromise between resolution and bandwidth. Since there is no correct analysis of the spatial heterodyne spectrometer in the literature, a derivation of the resolving power is given in the next section.

### 8.2 Resolving power

Figure 23 shows a footprint of the SHS, in which the optical paths of the two arms are projected onto a single optical axis, depicting the wavefront situation in the output arm. The incoming beam incident on the two gratings at Littrow angle  $\Theta_0$  is shown in figure 23a. Since we are dealing with *linear* optics, it is easier to represent incoherent light with a coherence length  $\ell_{coh}$  by a pulse of

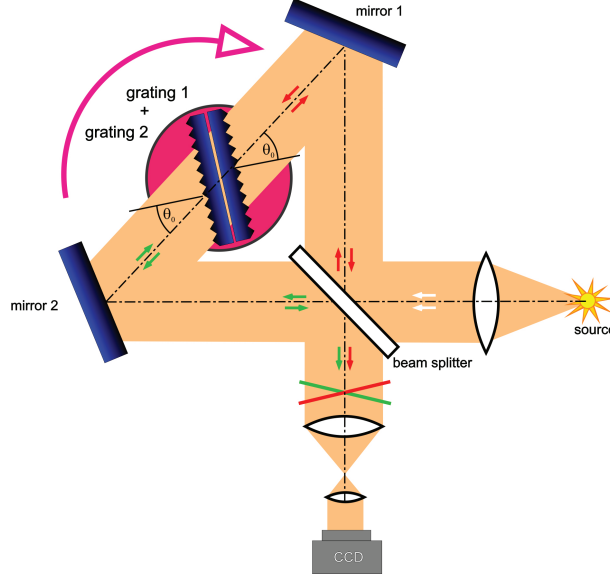


Figure 22: example of a single grating high resolution spectrometer.

duration  $\tau_{coh} = \ell_{coh}/c$ , where  $c$  is the speed of light. The side of the rectangle in the propagation direction (fig. 23a) is then  $c\tau_{coh}$ .

Figure 23b shows the situation in the output arm of the SHS for the wave packets centered at Littrow wavelength  $\lambda_0$ . Here, we neglect the fact that Fourier components that are off the Littrow wavelength (as definitely present in wave packet of finite length) are actually diffracted under a slightly different angle. Due to diffraction under Littrow angle and the resulting optical path difference between the two beam edges, the energy front is tilted with respect to the incoming energy front by an angle  $\gamma$ . This angle is given by (see Appendix):

$$\tan \gamma = 2 \tan \theta_0 \quad (18)$$

On a side note, Bor et al. [37] used the exact SHS configuration already in 1985 to construct a single-shot autocorrelator for ultrashort laser pulses. Here, the energy front is called pulse front for obvious reasons and actually used to laterally map a fringe-resolved autocorrelation function on detector with a single laser pulse. In this paper, a general expression for the energy front tilt in terms of angular dispersion  $d\epsilon/d\lambda$  was derived:

$$\tan \gamma = \lambda_0 \frac{d\epsilon}{d\lambda} \quad (19)$$

For incident radiation at  $\lambda_0 + \Delta\lambda$ , the diffracted beam is deflected from the optical axis by a small angle  $\Delta\alpha$  (with respect to the incident direction). The wavefront tilt (with respect to the direction of incidence) is  $\Delta\alpha$ , the energy front is tilted by a larger angle  $\gamma$  as given by equation 18. Although  $\gamma$  slightly changes for  $\Delta\alpha \neq 0$  (see Appendix), this change can be neglected for high-resolution versions of the SHS. The energy front tilt is in opposite directions for the two gratings (see Fig. 24b).

The projection  $p$  of the coherence width on the detecting image sensor, which is perpendicular

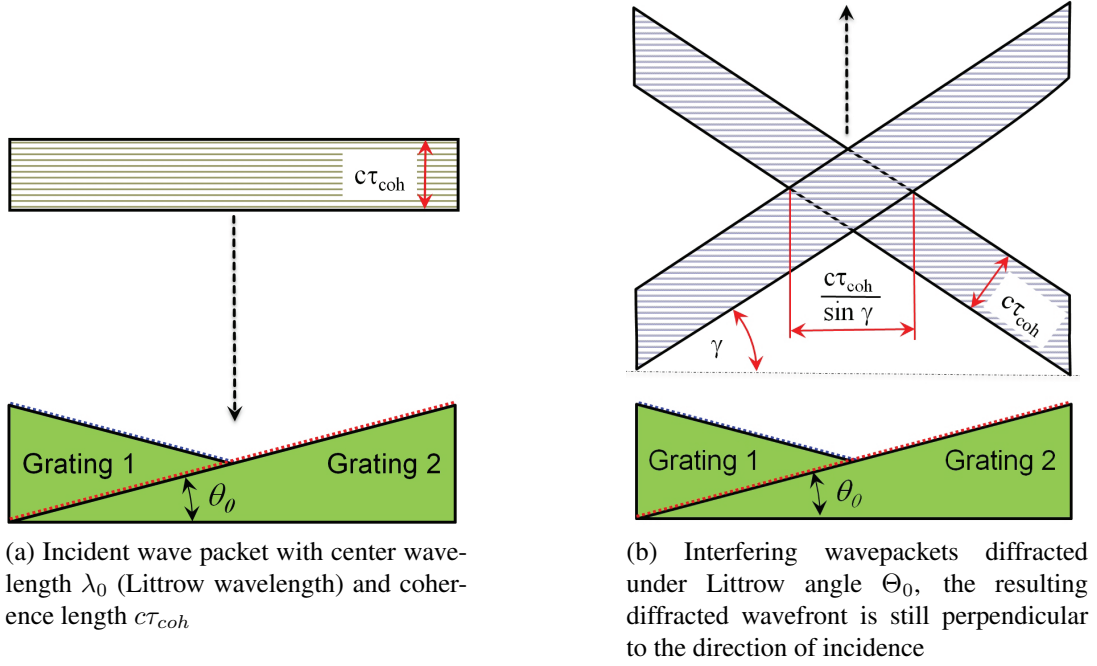


Figure 23: Diffraction at Littrow wavelength  $\lambda_0$

to the optical axis, is (from figure 24):

$$p = \frac{\ell_{coh}}{\sin \gamma} = \frac{c\tau_{coh}}{\sin \gamma} = \frac{\lambda_0^2}{\Delta\lambda_{coh} \sin \gamma}, \quad (20)$$

where  $\Delta\lambda_{coh}$  is the linewidth of the spectral emission line under investigation.

From this, we can deduce a criterion for the resolution of the SHS that is connected to the aperture of the whole system. If the width of the emission line is so small (i.e. the coherence time is so large) that the width of the fringe pattern  $p$  exceeds the aperture of the system  $A$ , the resolution limit is reached. This is, when:

$$A = p = \frac{\lambda_0^2}{\Delta\lambda_{coh} \sin \gamma},$$

This leads to the following expression for the resolving power:

$$R = \frac{\lambda}{\Delta\lambda} = \frac{A \sin \gamma}{\lambda_0}.$$

Presuming that we cannot resolve better than the linewidth anyway, we can write  $\Delta\lambda = \Delta\lambda_{coh}$ . Taking into account equation 18, the Littrow condition and the fact that the total number of grating grooves  $N$  within the aperture  $A$  is given by  $N = A g / \cos \theta_0$ , we get

$$R = N \cos \gamma, \quad (21)$$

with  $\gamma$  related to the Littrow angle  $\theta_0$  by equation (18).

Given the fact that  $\gamma > 0$  is necessary to have angular dispersion in the first place, this is less than a quarter of the value found in the literature [36, 38] and decreases further with increasing

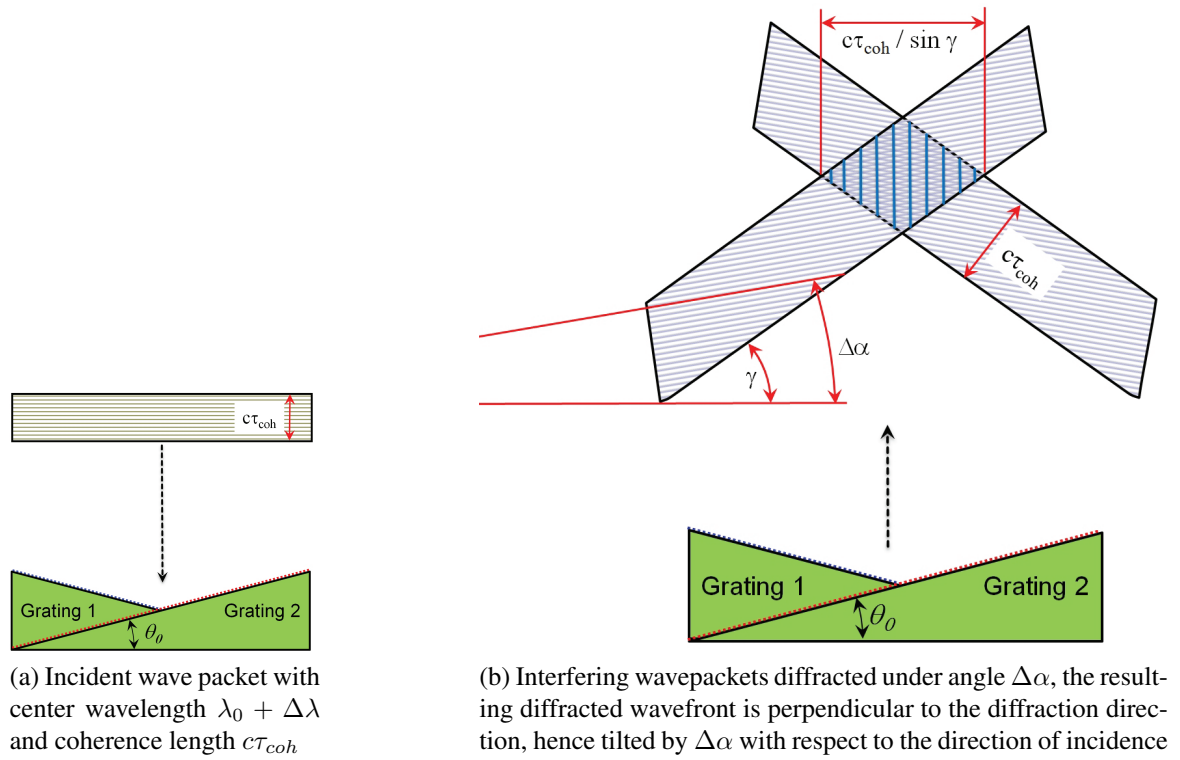


Figure 24: Diffraction at a wavelength  $\lambda_0 + \Delta\lambda$

Littrow angle which is tantamount to increasing resolution. Clearly, a compromise that has to be made for finding the optimum resolving power. A resolving power in the order of  $N$  was observed in [38], but was attributed to the low quality of the utilized optics.

### 8.3 Technical details

The holographic symmetric reflection gratings were of size  $34 \times 34 \text{ mm}^2$  with a groove density of 3000/mm. We used superpolished 100-mm square mirrors with a UV-enhanced aluminum coating and a custom-made beam splitter (Layertec GmbH, Germany) with a reflectivity of  $(50 \pm 8) \%$  for unpolarized light over the wavelength range 230-530 nm. The resulting clear aperture of the SHS was 25 mm up to a grating angle of  $\theta_0 = 42^\circ$ .

Attention has to be paid to make the two arms of the interferometer of equal length, for which purpose the grating including the rotation stage were placed on a translating mount parallel to the optical axis.

Using a 50-mm focal length UV fused silica lens, the grating surface was imaged onto a UV-sensitive CCD camera (JAI Inc. CM-140 GE-UV) while demagnifying the image by a factor of 4 to fit the 6-mm wide CCD chip.

The incoming light was collimated by using a fiber with a N.A. of 0.22 and an off-axis parabolic mirror (100 mm,  $90^\circ$ , UV-enhanced aluminum).

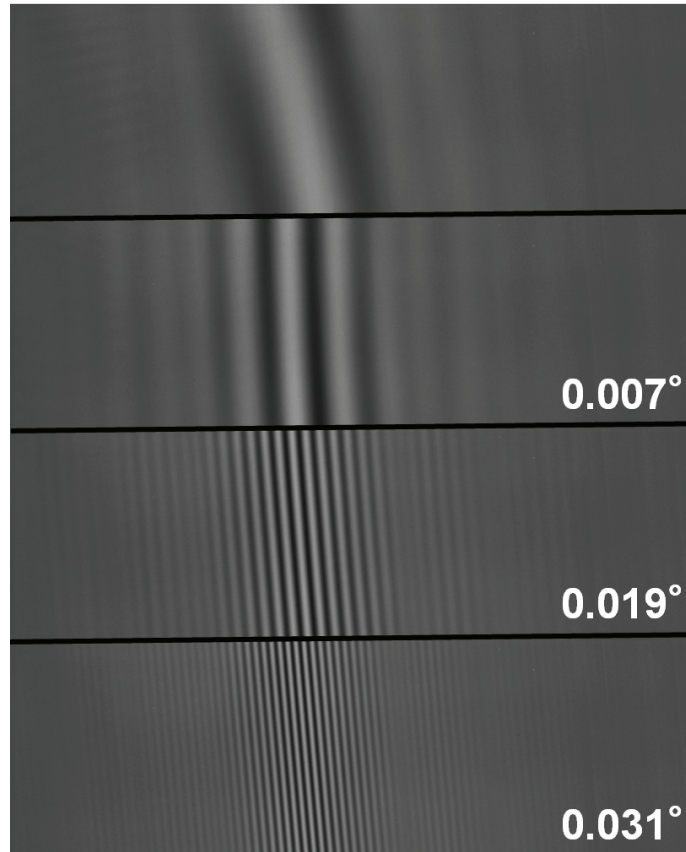


Figure 25: Four interferograms obtained with the folded SHS at grating angles  $22.344^\circ$ ,  $22.351^\circ$ ,  $22.363^\circ$ , and  $22.375^\circ$ , respectively. The numbers in the pictures are the angle difference to the top image. The light source is a Hg lamp, the angles correspond to the emission line at 253.65 nm. The slight tilt is due to imperfections in the gratings' rotation.

## 8.4 Resolution demonstration

Figure 25 shows the interferogram recorded by the CCD camera for 4 slightly different angles of the two gratings. The light source is a Hg calibration lamp (Stellarnet Inc.). From the Littrow condition, we know that the spectral line that forms the interferogram is the Hg line at 253.65 nm.

The most obvious feature is the envelope of the fringe pattern as predicted by figure 24b, the width of which does not change when the gratings are rotated. The total width of the image is 25 mm (taking into account the magnification before the camera), the half width of the envelope is 7.5 mm. Using equation (20), we can estimate the coherence time of the emission line to be  $\tau_{coh} = 16$  ps, which corresponds to a linewidth of 13 pm.

Another experiment was performed using a laser pointer that was labeled with an emission wavelength of 405 nm. The resulting interferogram is shown in figure 26, the beating between at least two neighboring emission lines can be clearly recognized. With a Fourier Transform and several image processing and averaging procedures, the spectrum shown in figure 27 was obtained. The red line denominates the Littrow angle that the SHS was set to. The spacing between the emission lines corresponds to a frequency difference of 133 GHz at this wavelength. Consequently, these lines are the longitudinal resonator modes of the InGaN laser diode with a length of about

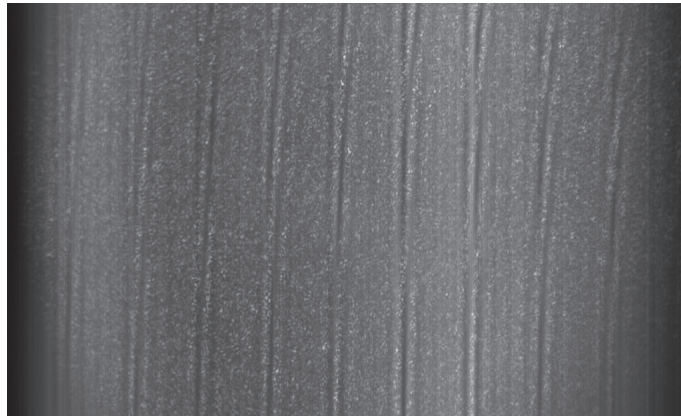


Figure 26: SHS interferogram of a nominal 405-nm diode laser showing the beating of neighboring emission lines.

1.1 mm.

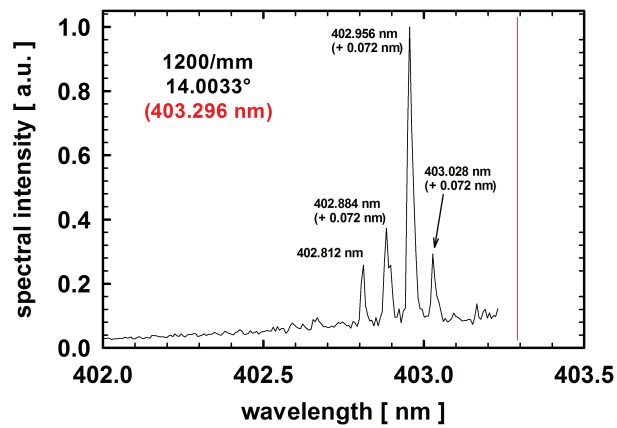


Figure 27: Spectrum of a nominal 405-nm diode laser derived from the interferogram in figure 26.



## References

- [1] D.R. Norman, J.L. Jones, K.J. Haskell, P.E. Vanier, and L. Forman. Active nuclear material detection and imaging. *IEEE Nuclear Science Symposium*, 49:1004–1008, 2006.
- [2] K.P. Ziock, W.W. Craig, L. Fabris, R.C. Lanza, S. Gallagher, B.K.P. Horn, and N.W. Madden. Large area imaging detector for long-range passive detection of fissile material. *Transactions on Nuclear Science*, 51(5):2238–2244, 1 August 2004.
- [3] Olivier J. Chalus, A. Sukhinin, A. Aceves, and J.-C. Diels. Propagation of non-diffracting intense ultraviolet beams. *Optics Communication*, 281:3356–3360, 2008.
- [4] Xiaozhen Xu and J.-C. Diels. Stable single-axial-mode operation of injection-seeded Q-switched Nd:YAG laser by real-time resonance tracking method. In *CLEO, 2013*, page CTh4I.8, San Jose, CA, 2013.
- [5] Xiaozhen Xu and J.-C. Diels. Stable single-axial-mode operation of injection-seeded Q-switched Nd:YAG laser by real-time resonance tracking method. *Applied Physics B*, 114:579, 2014.
- [6] Xiaozhen Xu. *High power UV source development and its applications*. PhD thesis, The University of New Mexico, Albuquerque, New Mexico, 2015y.
- [7] Xiaozhen Xu, Chengyong Feng, and J.-C. Diels. High energy pulse compression through two-pulse interaction mediated by stimulated brillouin scattering in liquid fluorocarbon. In *CLEO, 2013*, page CM3L.4, San Jose, CA, 2013.
- [8] Xiaozhen Xu, Chengyong Feng, and Jean-Claude Diels. Optimizing sub-ns pulse compression for high energy application. *Optics Express*, 22:13904–13915, 2014.
- [9] Chengyong Feng, Xiaozhen Xu, and Jean-Claude Diels. Generation of 300 ps laser pulse with 1.2 J energy by stimulated Brillouin scattering in water at 532 nm. *Opt. Lett.*, 39(12):3367–3370, Jun 2014.
- [10] Chengyong Feng, Xiaozhen Xu, and J.-C. Diels. Spatially-resolved pulse-front-tilt and pulse-width distribution of q-switched pulses from an unstable nd:yag resonator. In *CLEO, 2015*, pages JTh2A.24–1, San Jose, CA, 2015.
- [11] J.-C. Diels, J. Yeak, D. Mirell, R. Fuentes, S. Rostami, D. Faccio, and P. di Trapani. Air filaments and vacuum. *Laser Physics*, 20:1101–1106, 2010.
- [12] L. Arissian and J.-C. Diels. Ultrafast electron plasma index; an ionization perspective. *Journal of Lasers, Optics & Photonics*, 1:107–111, 2014.
- [13] Shermineh Rostami, J.-C. Diels, and L. Arissian. Polarization evolution of ultrashort pulses in air. *Optics Express*, 23:3299–3307, 2015.
- [14] Shermineh Rostami, Michael Chini, Khan Lim, John P. Palastro, Magali Durand, Jean-Claude Diels, Ladan Arissian, Matthieu Baudelet, and Martin Richardson. Dramatic enhancement of supercontinuum generation in elliptically-polarized laser filaments. arXiv:1505.01199, 2015.

- [15] A. Brodeur, C. Y. Chien, F. A. Ilkov, S. L. Chin, O. G. Kosareva, and V. P. Kandidov. Moving focus in the propagation of ultrashort laser pulses in air. *Optics Lett.*, 22:304–306, 1997.
- [16] A. Couairon and A. Mysyrowicz. Femtosecond filamentation in transparent media. *Physics Reports*, 441:49–189, 2007.
- [17] M. Mlejnek, E. M. Wright, and J. V. Moloney. Dynamic spatial replenishment of femtosecond pulse propagating in air. *Opt. Lett.*, 23:382–384, 1998.
- [18] A. Dubietis, E. Gaisauskas, G. Tamosauskas, and P. Di Trapani. Light filaments without self-channeling. *Phys. Rev. Lett.*, 92:253903–1—253903–5, 2004.
- [19] Andreas Velten, Andreas Schmitt-Sody, Shermin Rostami, Amin Rasoulof, Chengyong Feng, Jean-Claude Diels, and Ladan Arissian. Movies of plasmas and light filaments. *Journal of Physics B: Atomic, Molecular and Optical Physics*, 48:094020, 2015.
- [20] E. Freysz, M. Afifi, A. Ducasse, B. Pouligny, and J. R. Lalanne. Critical microemulsions as optically nonlinear media. *Journal of the Optical Society of America B*, 1:433, 1984.
- [21] E. P. Silaeva, S. A. Shlenov, and V. P. Kandidov. Multifilamentation of high-power femtosecond laser pulse in turbulent atmosphere with aerosol. *Appl. Phys. B*, 101:393–401, 2010.
- [22] M. Kolesik and J. V. Moloney. Self-healing fs light filaments. *Optics Lett.*, 29:590–592, 2004.
- [23] E. S. Efimenko, Y. A. Malkov, A. A. Murzanev, and A. N. Stepanov. Femtosecond laser pulse-induced breakdown of a single water microdroplet. *J. Opt. Soc. Am. B*, 31:534–541, 2014.
- [24] H. C. Bryant and N. Jarmie. The Glory. *Scientific American*, 231:60–71, 1974.
- [25] Ladan Arissian, Daniel Mirell, Shermin Rostami, Aaron Bernstein, Daniele Faccio, and Jean-Claude Diels. The effect of propagation in air on the filament spectrum. *Optics Express*, 20:8337–8343, 2012.
- [26] J. H. Odnher, D.A. Romanov, and R. J. Levis. Observation of impulsively stimulated vibrational Raman from filamentation in air. In *Proceedings of the SPIE Photonics West Conference 2010*, volume 7582, page 75820M, San Jose, CA, 2010.
- [27] J. H. Odnher, E. McCole, and R. J. Levis. Filament-driven impulsive raman spectroscopy. *J. Phys. Chem. A*, 115:13407, 2011.
- [28] J. Yu, D. Mondelain, G. Ange, R. Volk, S. Niedermeier, and J. P. Wolf. Backward supercontinuum emission from a filament generated by ultrashort laser pulses in air. *Optics Letters*, 26:533–535, 2001.
- [29] A.C. Bernstein, T.S. Luk, T.R. Nelson, A. McPherson, J.-C. Diels, and S.M. Cameron. Asymmetric ultra-short pulse splitting measured in air using frog. *Applied Physics B (Lasers and Optics)*, B75(1):119 – 122, July 2002.

- [30] W. Boyd. *Nonlinear Optics*. Academic Press, New York, 1991.
- [31] A. Sukhinin, A. B. Aceves, J.-C. Diels, and L. Arissian. On the co-existence of ir and and uv optical filaments. *J. Phys. B: At. Mol. Opt. Phys.*, 48:094021, 2015.
- [32] J. H. Odnher, D.A. Romanov, and R. J. Levis. Rovibrationalwave-packet dispersion during femtosecond laser filamentation in air. *Phys. Rev. Lett.*, 103:075005, 2009.
- [33] Chengyong Feng, Jean-Claude Diels, Xiaozhen Xu, and Ladan Arissian. Ring-shaped backward stimulated raman scattering driven by stimulated brillouin scattering. *Optics Express*, 23:17035–17045, 2015.
- [34] V. Boutou, C. Favre, S.C.Hill, Y.L. Pan, R.K. chang, and J.P. Wolf. Backward enhanced emission from multiphoton processes in aerosols. *Applied Physics B*, 75:145–152, 2002.
- [35] A. Briand W. Pietsch, A. Petit. Isotope ratio determination of uranium by optical emission spectroscopy on a laser-produced plasma; basic investigation and analytical results. *Spectrochimica Acta Part B*, 53:751–761, 1998.
- [36] J. Harlander, R. J. Reynolds, and F. L. Roesler. Spatial heterodyne spectroscopy for the exploration of diffuse interstellar emission lines at far-ultraviolet wavelengths. *Astrophysical Journal*, 396:730, 1992.
- [37] Z. Bor and B. Rácz. Group velocity dispersion in prisms and its application to pulse compression and travelling-wave excitation. *Optics Communications*, 54(3):165 – 170, 1985.
- [38] N. Gomer, Ch. M. Gordon, P. Lucey, Sh. K. Sharma, J. Ch. Carter, and S. M. Angel. Raman spectroscopy using a spatial heterodyne spectrometer: Proof of concept. *Applied Spectroscopy*, 65(9):849 – 857, 2011.

**DISTRIBUTION LIST**  
**DTRA-TR-16-66**

**DEPARTMENT OF DEFENSE**

DEFENSE THREAT REDUCTION  
AGENCY  
8725 JOHN J. KINGMAN ROAD  
STOP 6201  
FORT BELVOIR, VA 22060  
ATTN: D. PETERSEN

DEFENSE TECHNICAL  
INFORMATION CENTER  
8725 JOHN J. KINGMAN ROAD,  
SUITE 0944  
FT. BELVOIR, VA 22060-6201  
ATTN: DTIC/OCA

**DEPARTMENT OF DEFENSE  
CONTRACTORS**

QUANTERION SOLUTIONS, INC.  
1680 TEXAS STREET, SE  
KIRTLAND AFB, NM 87117-5669  
ATTN: DTRIAC